RSC Advances

ROYAL SOCIETY OF CHEMISTRY

PAPER

View Article Online
View Journal | View Issue

Check for updates

Cite this: *RSC Adv.*, 2025, **15**, 7489

Intermolecular interaction of Al_8O_{12} oxymetallic clusters in the detection of atmospheric pollutants: a DFT exploration of CO, CO_2, H_2, N_2, NO, NO_2, O_2, and SO_2, binding mechanisms†

Sajida Riffat Laraib,[a] Ji Liu,*[a] Yuan-gu Xia,[a] Yang-wen Wu,[a] Mohsen Doust Mohammadi,[bc] Nayab Fatima Noor[d] and Qiang Lu[a]

Received 10th November 2024
Accepted 5th February 2025

DOI: 10.1039/d4ra07985j

rsc.li/rsc-advances

Due to the lack of inherent geometric symmetry present in the structures of aluminum oxide clusters, determining their stable configuration becomes an exceedingly formidable task computationally. In this comprehensive analysis, we first propose the most stable state of Al_8O_{12}, determined through Density Functional Theory calculations at ωB97XD/Def2-TZVP level of theory. Multiple structural isomers were scrutinized for their stability and spin state, with the optimal structure determined using the bee colony algorithm for global optimization. Furthermore, we investigated the intermolecular interactions between various atmospheric gases (CO, CO_2, H_2, N_2, NO, NO_2, O_2, and SO_2) and this oxymetallic cluster. The interactions were evaluated through adsorption energy (E_{ads}) calculations and characterized using multiple analytical frameworks: quantum theory of atoms in molecules, total density of states, natural bond orbital analysis (including bond orders, natural charges, and natural electron configurations), and non-covalent interaction analysis with reduced density gradient. The findings reveal robust interactions between the gas molecules and the cluster structure, with the cluster exhibiting remarkable potential for monitoring various atmospheric gases. Adsorption energy calculations reveal a decreasing trend in binding strength for various gases on the Al_8O_{12} cluster, with values of SO_2 (−1.283 eV) > CO (−0.669 eV) > CO_2 (−0.579 eV) > NO_2 (−0.573 eV) > O_2 (−0.521 eV) > NO (−0.486 eV) > N_2 (−0.432 eV) > H_2 (−0.239 eV), indicating the cluster's potential for selective gas adsorption in applications like sensing and environmental monitoring. The calculated adsorption energies suggest this cluster holds great promise for the development of gas sensing and removal devices, particularly for environmental monitoring applications.

1. Introduction

Computational chemistry has fundamentally transformed the landscape of chemical research, establishing itself as a cornerstone in modern scientific investigation. By bridging theoretical predictions with experimental observations, it provides unprecedented insights into molecular and materials behavior at the atomic scale.[1,2] The implementation of theoretical chemistry methods has become indispensable across diverse scientific and industrial applications. In environmental monitoring, computational approaches have enabled detailed understanding of greenhouse gas capture mechanisms, particularly in metal–organic frameworks (MOFs) and zeolites.[3,4] Similarly, in sensor technology development, theoretical predictions have guided the design of highly selective gas sensors based on 2D materials like graphene and MXenes.[5] These applications rely heavily on accurate predictions of fundamental properties, including adsorption energies, electronic structure, and charge transfer mechanisms. Density Functional Theory (DFT) has emerged as the method of choice among computational approaches, offering an optimal balance between accuracy and computational efficiency.[6–8] Its success in treating electron correlation effects while maintaining reasonable computational costs has made it particularly valuable for studying complex systems. For instance, DFT calculations have been instrumental in understanding CO_2 capture in amine-functionalized MOFs,[9,10] predicting binding energies and structural changes upon gas adsorption. In gas sensing

---

[a] *National Engineering Research Center of New Energy Power Generation, North China Electric Power University, Beijing 102206, P. R. China. E-mail: liujipower@ncepu.edu.cn; liujipower@126.com*

[b] *School of Chemistry, College of Science, University of Tehran, Tehran 14176, Iran*

[c] *Climate and Atmospheric Research Centre, The Cyprus Institute, 20, Konstantinou Kavafi Street, Nicosia 2121, Cyprus*

[d] *Military College of Signals, National University of Science and Technology, Rawalpindi, Pakistan*

† Electronic supplementary information (ESI) available. See DOI: https://doi.org/10.1039/d4ra07985j

applications, DFT has enabled detailed analysis of the electronic properties of sensing materials, explaining phenomena such as conductivity changes upon target gas adsorption.[11–13] The impact of computational chemistry extends beyond basic research into practical applications. In materials design, DFT-based screening has accelerated the discovery of new gas separation membranes and sensing materials, reducing the time and resources required for experimental testing. This approach has led to the identification of promising candidates for selective gas capture, such as functionalized covalent organic frameworks (COFs) and novel 2D materials for gas sensing applications.[14–17]

Metallic clusters have engendered considerable attention in nanomaterials due to their idiosyncratic properties and prospective applications in diverse industries.[18] Among these clusters, aluminum oxide (Al_8O_{12}) clusters emerge as a captivating subject of inquiry. Aluminum oxide exhibits extraordinary attributes, such as elevated thermal stability, mechanical robustness, and chemical inertness, endowing it with an ideal candidacy for a myriad of technological applications.[19,20] Elucidating the structure of aluminum clusters assumes paramount importance as it indubitably impinges upon their properties and reactivity. Previous investigations have illumined the fundamental traits of aluminum oxide clusters, but further research is indisputably warranted to exhaustively explore their multifarious characteristics.[21] The synthesis of aluminum oxide clusters can be effected through a gamut of methods.[19,22–32]

The forthcoming challenge in the theoretical investigation of metal clusters comprising aluminum and oxygen atoms lies in their lack of adherence to specific crystallographic order and geometric symmetry.[33] As a consequence, the number of structural isomers under consideration for these clusters can vary significantly based on the number of atoms involved.[34] Consequently, the exhaustive exploration of each isomer becomes an arduous task, necessitating it nonetheless due to the absence of any definitive logic that can determine nature's preference for a particular isomer.[35] The determination of structures revolves around comprehending the spatial arrangement of atoms and verifying the system's total energy. Furthermore, accounting for spin multiplicity assumes importance since identifying the ground state's spin state remains uncertain. Consequently, the enormity of the systems under scrutiny, when incorporating these parameters, may demand substantial computational power and resources. Nevertheless, the employment of artificial intelligence and pioneering algorithms has somewhat smoothed the path, enabling the identification of the geometric structure of aluminum oxide clusters with 8 aluminum atoms and 12 oxygen atoms. Given that such clusters often lack symmetrical spatial configurations, investigating the interaction between these clusters and a polluting gas demands considering the cluster's surroundings. Consequently, the gas molecule's approach to the cluster from any point and the investigation of their interaction energy add further complexity to the task. Thankfully, the incorporation of artificial intelligence in the ABCluster[36] software has facilitated progress in this area, culminating in the attainment of the global minimum, thus offering a valuable resource for research.

This study investigates the stability and adsorption behavior of the Al_8O_{12} cluster, calculated through density functional theory at the ωB97XD/Def2-TZVP level. The optimized Al_8O_{12} configuration, identified using the bee colony algorithm, serves as a robust framework for analyzing interactions with various atmospheric gases, including CO, CO_2, H_2, N_2, NO, NO_2, O_2, and SO_2. Key insights emerge from comprehensive analyses of electronic and thermodynamic parameters, including zero-point energy (ZPE), thermal energy (TE), heat capacity (C_V), and entropy (S), revealing molecular trends in vibrational coupling and thermal energy storage. Adsorption energy (E_{ads}) calculations show a descending trend in binding strength as SO_2 (−0.0472 Ha) > CO (−0.0246 Ha) > CO_2 (−0.0213 Ha) > NO_2 (−0.0211 Ha) > O_2 (−0.0192 Ha) > NO (−0.0179 Ha) > N_2 (−0.0159 Ha) > H_2 (−0.0088 Ha), correlating stronger binding with electron-accepting capability and molecular properties. Analyses through Quantum Theory of Atoms in Molecules (QTAIM), Density of States (TDOS), Natural Bond Orbital (NBO), and Non-Covalent Interaction (NCI) underscore Al_8O_{12}'s selective adsorption potential, suggesting applications in gas sensing and environmental monitoring technologies.

2. Computational details

The ωB97XD[37] functional is a widely used hybrid density functional that incorporates long-range corrections and a dispersion term (XD) to accurately model non-covalent interactions such as hydrogen bonding and dispersion forces, making it ideal for studying systems like the Al_8O_{12} cluster and its interactions with atmospheric pollutants. Its computational efficiency and ability to capture subtle binding effects make it particularly effective for modeling both strong covalent bonds and weak intermolecular interactions. The functional has been successfully used in various cluster studies, demonstrating its reliability in predicting structural, electronic, and interaction properties.[38–40] The Def2-SVP and Def2-TZVP basis sets,[41] chosen for their balance of accuracy and computational efficiency, are commonly used in quantum calculations. Def2-SVP, a double-zeta basis set, is suitable for preliminary calculations or large systems, while Def2-TZVP, a triple-zeta basis set, provides greater accuracy for systems with more complex electronic environments. These basis sets have been successfully applied in studies of aluminum clusters, making them well-suited for modeling the Al_8O_{12} cluster and its interactions with atmospheric gases like CO, CO_2, NO_2, and SO_2, ensuring accurate depictions of charge density and intermolecular interactions.[42–45]

Supramolecular theory[46,47] in adsorption energy calculation focuses on understanding the non-covalent interactions between guest molecules and host surfaces or receptors, which include van der Waals forces, hydrogen bonding, and π–π interactions. The adsorption energy is a measure of the strength of this binding interaction, with lower values indicating weaker binding and higher values indicating stronger interactions. The process of calculating adsorption energy involves several steps:

First, the geometries of the guest molecule and the host surface are optimized using quantum chemical methods. Next, a supramolecular complex is formed by bringing the guest molecule close to the host surface. The total energy of this complex is then calculated, considering both electronic energy and intermolecular interactions. Reference calculations are performed to obtain accurate adsorption energy values. These include calculating the isolated guest molecule and host surface energies in their respective gas-phase states. The adsorption energy (E_{ads}) is then obtained as the difference between the total energy of the supramolecular complex and the sum of the energies of the isolated guest molecule and host surface. A negative adsorption energy ($E_{\text{ads}} < 0$) signifies energetically favorable adsorption, indicating stable interactions between the guest and host. Conversely, a positive adsorption energy ($E_{\text{ads}} > 0$) suggests an unfavorable interaction, meaning the guest molecule is weakly bound to the host surface.

$$E_{\text{ads}} = E_{\text{complex}} - (E_{\text{guest}} + E_{\text{host}}) + \Delta E_{\text{ZPE}} \tag{1}$$

Here, complex molecule is the combination of gas/Al_8O_{12} molecules; E_{guest} indicates the total energy of isolated gas and E_{host} denotes the total energy of Al_8O_{12} molecule in an isolated condition. Also, ΔE_{ZPE} specifies the zero-point energy correction. The Gaussian 16, Revision C.01 (ref. 48) software was employed for conducting geometric optimization calculations, while NBO calculations were executed using the NBO 3.1 software[49] integrated into the Gaussian package. The resultant NBO outputs were utilized for conducting QTAIM analysis. For bond order calculations and topology analysis, the Multiwfn[50] software was applied. Additionally, ABCluster[36] was utilized for preparing primary structures. Furthermore, GaussView[51] and Chemcraft were employed to prepare input files and figures, respectively.

3. Result and discussion

3.1. Geometry optimization

As mentioned in the previous section, the first step involves the geometric optimization of gas molecules and the aluminum oxide cluster. For gases such as NO, NO_2, CO, CO_2, SO_2, H_2, N_2, O_2, and SO_2, extensive information is readily available from both experimental and theoretical sources across various databases, allowing the initial geometric parameters to be set based on established data before initiating the optimization process. This approach ensures accuracy and reliability in the starting configurations of these molecules. However, a more complex aspect of this research is the structural optimization of the Al_8O_{12} cluster,[52] which requires precision in arranging oxygen and aluminum atoms in space. ABCluster software is employed to determine these atomic positions using *XYZ* coordinates, with optimization guided by the bee colony algorithm integrated into the software. This approach relies on the Coulomb–Born–Mayer potential (U_{CBM}) model,[53] which includes two critical parameters, B and ρ. These parameters, specifically calibrated for the aluminum–oxygen interaction, have been sourced from relevant literature, providing a well-defined potential for accurately modeling the Al_8O_{12} structure and ensuring a reliable basis for adsorption studies of various gas pollutants (Fig. 1).[54]

$$U_{\text{CBM}} = \sum_{i=1}^{N}\sum_{i<j}^{N}\left(\frac{e^2}{4\pi\varepsilon_0}\frac{q_i q_j}{r_{ij}} + B_{ij}\exp\left(-\frac{r_{ij}}{\rho_{ij}}\right)\right) \tag{2}$$

Various initial configurations of the Al_8O_{12} molecule were examined, displaying distinct variations in bond lengths, bond angles, and dihedral angles. The primary focus, however, is on assessing the stability of these configurations. To address this, numerous configurations underwent geometric optimization using the ωB97XD/def2-SVP method. From this set, the configuration with the lowest total energy was identified as the most stable isomer and chosen as the representative structure in this study. Post-optimization, vibrational frequency calculations confirmed that this optimized structure represents a true local minimum on the potential energy surface, as evidenced by the absence of negative or imaginary frequencies. Among the various configurations of the isolated cluster in local minimum states, the system with the lowest energy was selected and re-optimized using ωB97XD/def2-TZVP method. The results of optimization and vibrational frequency calculations are compiled in Table 1. In the present study, the absence of imaginary frequencies was checked to ensure that the stationary points obtained correspond to minima on the potential energy surface. This was confirmed by the positive vibrational frequencies observed, as shown in Fig. 2. Additionally, this figure illustrates the molecule's highest infrared (IR) activity within the infrared range. Fig. 3 depicts the optimized gas molecules, highlighting bond angles and bond distances. The equilibrium bond distance for the CO molecule is 1.12 Å, while for the CO_2 molecule, it is 1.16 Å between the oxygen and carbon atoms. In the case of H_2, the bond distance is 0.74 Å. For N_2, it measures 1.09 Å, whereas O_2 exhibits a bond distance of 1.19 Å, and the equilibrium bond distance in NO is 1.14 Å. Furthermore, the triatomic molecules such as NO_2 have a bond distance of 1.18 Å and a bond angle of 134.5°, while for SO_2, these values are 1.43 Å and 118.91°, respectively.

The bond distances and atomic angles for molecules such as H_2, SO_2, NO, NO_2, CO, CO_2, O_2, and N_2 have been experimentally determined and are essential for understanding their molecular properties. For H_2, the bond distance is 0.7414 Å.[55] In the case of O_2, the bond distance is 1.208 Å.[55] In SO_2, the S═O bond length is 1.434 Å with an O═S═O angle of 119.3°.[56] NO has a bond distance of 1.150 Å,[55] while in NO_2, the N═O bond measures 1.152 Å, and the O═N═O angle is 134.0°.[55] The bond distance in CO is 1.128 Å,[55] and CO_2 exhibits a C═O bond of 1.161 Å with a linear O═C═O angle of 180.0°.[57] Finally, the bond distance in N_2 is 1.098 Å.[55] These experimentally obtained values are crucial for accurate molecular modeling and understanding the interactions within these molecules. The experimentally studied bond distances and atomic angles for molecules are reported above. Our calculated values for these molecules are depicted in Fig. 3, allowing for a direct comparison with the experimental data.

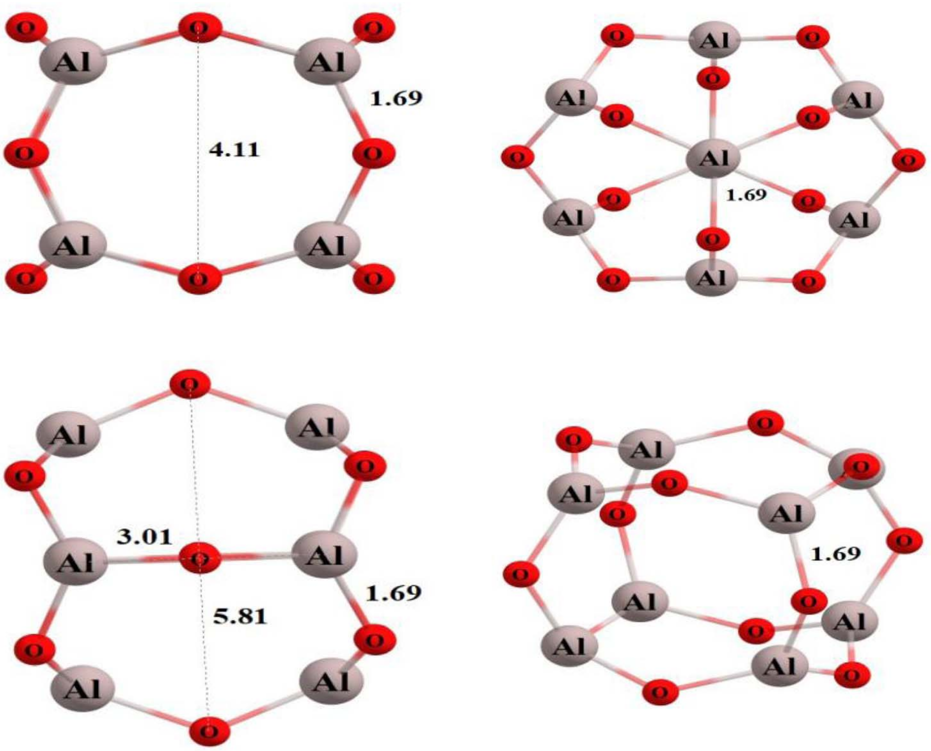

Fig. 1 The optimized structure of the Al_8O_{12} cluster in different orientations was obtained at ωB97XD/Def2-TZVP level of theory. The values of bond length are in Å.

In the subsequent stage, gas molecules were systematically arranged around the aluminum oxide cluster at various distances and orientations to ensure a thorough sampling of potential adsorption scenarios. The initial conformers of the gas/cluster configurations were generated using the ABCluster software, which employs a global optimization method to explore a diverse range of isomeric forms. Each conformer was first optimized using the ωB97XD/Def2-SVP method, allowing for a reliable assessment of their geometric stability. Following this, the most stable conformer from this initial optimization

Table 1 The values of electronic energies, including the zero-point energy correction (EE in hartree), zero-point energy (E_{ZPE}) correction (hartree), thermal energy (TE) in kcal mol^{-1}, heat capacity (C_V) in cal mol^{-1} K^{-1}, entropy (S) in cal mol^{-1} K^{-1}, and adsorption energies (E_{ads}) in eV, calculated at the ωB97XD/Def2-TZVP level of theory. The notation gas@Al_8O_{12}_*x*, where 'gas' refers to CO, CO_2, H_2, N_2, NO, NO_2, O_2, and SO_2, and the '@' symbol indicates that the gas is adsorbed onto the Al_8O_{12} cluster. The index '*x*' refers to the number of the most energetically stable gas/cluster configuration

Systems	EE	E_{ZPE}	TE	C_V	S	E_{ads}
Al_8O_{12}	−2843.626074	0.062431	51.77	73.304	144.385	—
CO	−113.3216803	0.005120	4.694	4.973	47.183	—
CO_2	−188.6055738	0.011925	9.115	6.774	50.983	—
H_2	−1.176166786	0.010112	7.826	4.968	31.139	—
N_2	−109.5325359	0.005686	5.050	4.970	45.722	—
NO	−129.9015575	0.004634	4.390	4.978	48.996	—
NO_2	−205.0959442	0.009096	7.543	6.761	57.233	—
O_2	−150.2784895	0.003889	3.923	5.004	46.757	—
SO_2	−548.6529637	0.007306	6.499	7.403	59.204	—
CO@Al_8O_{12}_17	−2956.972323	0.069691	58.263	82.459	160.867	−0.0246
CO_2@$A_{l8}O_{12}$_9	−3032.252992	0.075476	62.360	84.804	165.67	−0.0213
H_2@Al_8O_{12}_1	−2844.811008	0.076374	61.917	80.769	154.095	−0.0088
N_2@Al_8O_{12}_3	−2953.174555	0.069932	58.514	82.651	161.115	−0.0159
NO@Al_8O_{12}_9	−2973.545515	0.068512	57.819	82.867	165.521	−0.0179
NO_2@Al_8O_{12}_13	−3048.743161	0.073071	61.172	85.607	171.104	−0.0211
O_2@Al_8O_{12}_2	−2993.923789	0.067734	57.296	82.767	164.068	−0.0192
SO_2@Al_8O_{12}_2	−3392.326201	0.071847	59.983	85.557	162.819	−0.0472

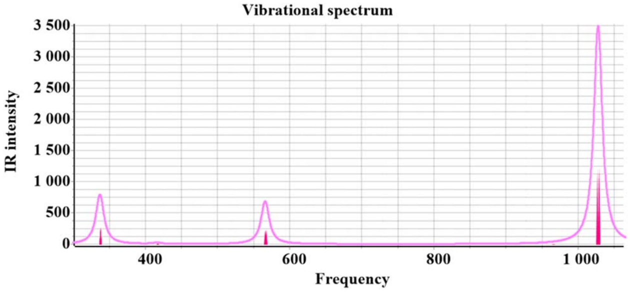

Fig. 2 Vibrational frequency spectrum of the isolated Al_8O_{12} cluster, displaying all stable (positive) vibrational modes. The x-axis represents the vibrational frequencies (cm^{-1}), while the y-axis shows the corresponding IR intensities ($km\ mol^{-1}$). Peaks denote distinct vibrational modes, with intensity values reflecting the relative strength of IR absorption. Vibrational frequency calculations are performed at ωB97XD/Def2-TZVP level of theory.

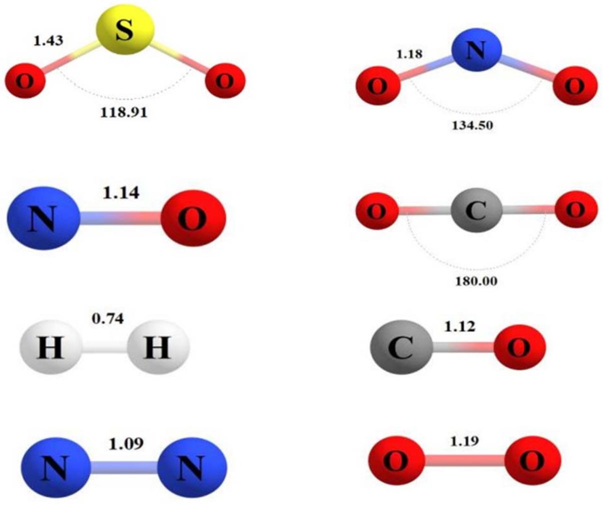

Fig. 3 The optimized structure of the gases. The calculations are performed at ωB97XD/Def2-TZVP level of theory. The values of bond length are in Å and atomic angle in radians.

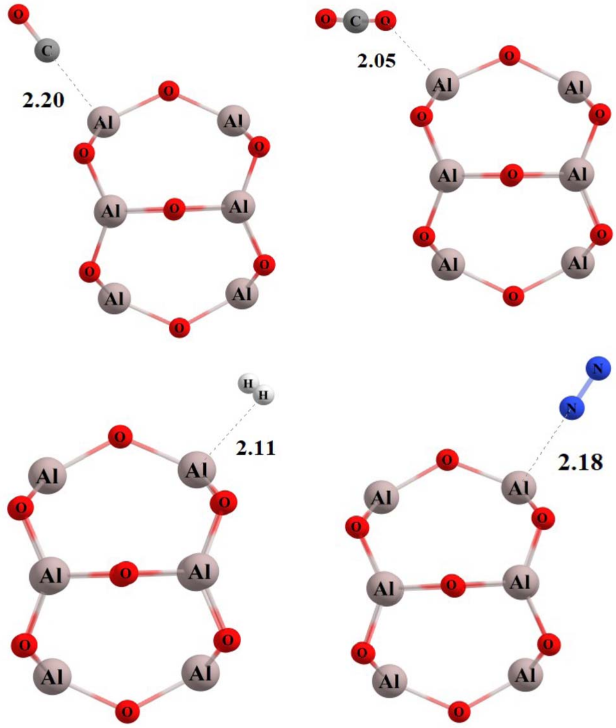

Fig. 4 Optimized structures of gas molecules CO, CO_2, H_2, and N_2 adsorbed on the outer surface of the Al_8O_{12} cluster. Calculations were performed at the ωB97XD/Def2-TZVP level of theory. Bond lengths are presented in Å.

was subjected to a further refinement using the more computationally demanding ωB97XD/Def2-TZVP method, which provides a higher level of accuracy. This step ensured that the optimized structure truly represents a global energy minimum on the potential energy surface. The adsorption energy for each configuration was then computed using eqn (1), with the configuration yielding the highest adsorption energy considered the most stable gas/cluster state. Table S1 in ESI† file summarizes the calculated adsorption energies for the 20 most stable configurations, each indexed as gas@cluster_*x*, while Table S3† provides the corresponding *XYZ* coordinates for these configurations. Importantly, the reported energy values include zero-point energy corrections, enhancing the data's accuracy and reliability. This comprehensive approach ensures a robust analysis of the interaction dynamics between the gas molecules and the aluminum oxide cluster, facilitating insights into their adsorption properties. Table 1 lists the configurations with the highest energy stability among the 20 studied samples for each gas with the cluster, where their respective indices are specified as gas@cluster_*x*. Fig. 4 and 5 have been created to illustrate the equilibrium distances of the interactions between the gases and the cluster. Since it is not feasible to display all bond angles and distances in a single figure, the most effective way to present this information is through an *XYZ* coordinates, which is provided in Table S4 in ESI† section.

The comprehensive analysis of electronic energies and thermodynamic parameters reveals significant insights into the behavior of molecular species and their interactions with the Al_8O_{12} cluster system. The hierarchical stability pattern, with the Al_8O_{12} cluster demonstrating remarkable stability at −2843.626074 hartree, underscores the influence of optimized geometric configurations and balanced electronic structures, where aluminum and oxygen atoms form a robust framework through strong covalent bonds. Among the examined molecules, the trend in electronic energies—SO_2 (−548.6529637 Ha) > CO_2 (−188.6055738 Ha) > O_2 (−150.2784895 Ha) > NO_2 (−205.0959442 Ha) > NO (−129.9015575 Ha) > CO (−113.3216803 Ha) > N_2 (−109.5325359 Ha) > H_2 (−1.176166786 Ha)—reflects key molecular characteristics such as molecular size, bond multiplicity, electronic configuration, and atomic composition. Upon adsorption, host–guest complex formation reveals energy changes like SO_2@Al_8O_{12}_2 at −3392.326201 Ha ($\Delta E = -0.0472$ Ha) and CO@Al_8O_{12}_17 at −2956.972323 Ha ($\Delta E = -0.0246$ Ha), with trends indicating that molecules with

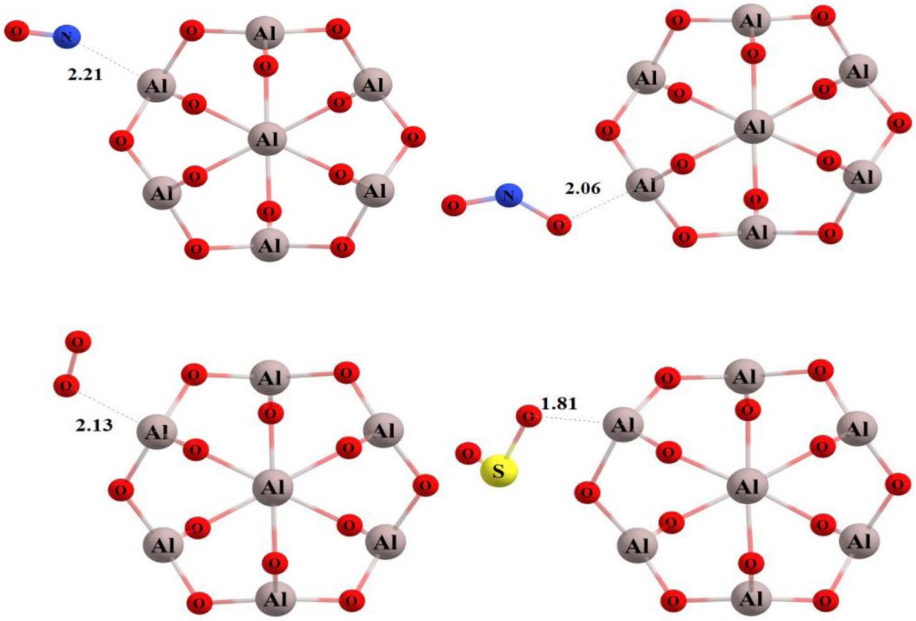

Fig. 5 Optimized structures of gas molecules NO, NO_2, O_2, and SO_2 adsorbed on the outer surface of the Al_8O_{12} cluster. Calculations were performed at the ωB97XD/Def2-TZVP level of theory. Bond lengths are presented in Å.

stronger electron-withdrawing properties, larger sizes, suitable orbital overlap, and higher polarizability demonstrate stronger binding energies. This stabilization pattern suggests multiple electronic interaction types—electrostatic, orbital hybridization, charge transfer, and van der Waals forces—affecting binding strengths, with electron-accepting capabilities of adsorbates correlating strongly with interaction strengths. Al_8O_{12}, as a versatile host, exhibits promising binding potential without compromising its electronic stability, thereby offering insights that can guide the prediction of adsorption behaviors and the design of advanced materials where electronic interactions are pivotal for functionality.

The examination of zero-point energies (ZPE) and vibrational characteristics reveals intricate quantum mechanical aspects of these systems, providing fundamental insights into the molecular dynamics and energy landscapes. The ZPE values of isolated molecules follow a logical progression in hartree units: O_2 (0.003889 Ha) < NO (0.004634 Ha) < CO (0.005120 Ha) < N_2 (0.005686 Ha) < SO_2 (0.007306 Ha) < NO_2 (0.009096 Ha) < H_2 (0.010112 Ha) < CO_2 (0.011925 Ha) < Al_8O_{12} (0.062431 Ha). This systematic progression directly correlates with the molecular degrees of freedom and vibrational mode complexity. Notably, H_2 exhibits a relatively high ZPE despite its structural simplicity, reflecting its characteristic high-frequency vibration due to its low reduced mass. The progression culminates with the Al_8O_{12} cluster, whose complex three-dimensional structure contributes to numerous vibrational modes and consequently a high ZPE value. Upon adsorption, all complexes demonstrate elevated ZPE values, displaying a distinct trend: $O_2@Al_8O_{12}\_2$ (0.067734 Ha) < $NO@Al_8O_{12}\_9$ (0.068512 Ha) < $CO@Al_8O_{12}\_17$ (0.069691 Ha) < $N_2@Al_8O_{12}\_3$ (0.069932 Ha) < $SO_2@Al_8O_{12}\_2$ (0.071847 Ha) < $NO_2@Al_8O_{12}\_13$ (0.073071 Ha) < $CO_2@Al_8O_{12}\_9$ (0.075476 Ha) < $H_2@Al_8O_{12}\_1$ (0.076374 Ha). This systematic increase in ZPE values indicates substantial modifications to the vibrational structure of both adsorbate and substrate. The magnitude of ZPE enhancement (ΔZPE) follows the trend: H_2 (0.003831 Ha) > CO_2 (0.001120 Ha) > NO_2 (0.001544 Ha) > SO_2 (0.002110 Ha) > N_2 (0.001815 Ha) > CO (0.001940 Ha) > NO (0.001447 Ha) > O_2 (0.001414 Ha), revealing distinct patterns in vibrational coupling strength.

These vibrational modifications are further manifested in the thermal energy (TE) values measured in kcal mol^{-1}. The isolated molecules show a clear trend: O_2 (3.923) < NO (4.390) < CO (4.694) < N_2 (5.050) < SO_2 (6.499) < NO_2 (7.543) < H_2 (7.826) < CO_2 (9.115) < Al_8O_{12} (51.77). Upon adsorption, all complexes exhibit systematically enhanced TE values: $O_2@Al_8O_{12}\_2$ (57.296) < $NO@Al_8O_{12}\_9$ (57.819) < $CO@Al_8O_{12}\_17$ (58.263) < $N_2@Al_8O_{12}\_3$ (58.514) < $SO_2@Al_8O_{12}\_2$ (59.983) < $NO_2@Al_8O_{12}\_13$ (61.172) < $H_2@Al_8O_{12}\_1$ (61.917) < $CO_2@Al_8O_{12}\_9$ (62.360). The TE enhancement (ΔTE) follows a distinct pattern: CO_2 (1.475) > NO_2 (1.859) > SO_2 (1.714) > H_2 (2.321) > N_2 (1.694) > CO (1.799) > NO (1.652) > O_2 (1.599) kcal mol^{-1}, indicating varying degrees of vibrational coupling strength. This comprehensive analysis reveals several key insights: (1) The ZPE and TE enhancements show nonlinear relationships with molecular mass and complexity, suggesting that electronic structure effects significantly influence vibrational coupling; (2) molecules with higher dipole moments generally show stronger vibrational coupling, indicating the importance of electrostatic interactions in modifying the potential energy surface; (3) the consistent increase in both ZPE and TE upon adsorption suggests the formation of new low-frequency vibrational modes at the adsorbate-substrate interface; (4) the magnitude of vibrational coupling correlates with binding strength, particularly for molecules with strong electron-accepting capabilities. These findings demonstrate that the Al_8O_{12} cluster effectively modifies the vibrational properties of adsorbed molecules while maintaining system stability.

The interplay between heat capacity (C_V) and entropy (S) provides deep insights into the thermodynamic behavior of these molecular adsorption systems, revealing complex relationships between structural features and energy storage mechanisms. The C_V values, measured in cal mol^{-1} K^{-1}, demonstrate a systematic increase upon adsorption, with complexes exhibiting values between 80.769 and 85.607, significantly higher than the isolated Al_8O_{12} (73.304). This enhancement pattern follows a distinct trend: H_2@Al_8O_{12}_1 (80.769) < CO@Al_8O_{12}_17 (82.459) < N_2@Al_8O_{12}_3 (82.651) < O_2@Al_8O_{12}_2 (82.767) < NO@Al_8O_{12}_9 (82.867) < SO_2@Al_8O_{12}_2 (85.557) < NO_2@Al_8O_{12}_13 (85.607) < CO_2@Al_8O_{12}_9 (84.804). The systematic increase in C_V can be attributed to several factors: (1) the introduction of new vibrational modes at the adsorbate-substrate interface, (2) modification of existing molecular vibrations due to electronic interactions, and (3) coupling between adsorbate rotational modes and substrate phonons. Notably, molecules with higher degrees of freedom and stronger electronic interactions with the substrate (NO_2, CO_2, SO_2) show larger C_V enhancements, suggesting that both structural complexity and electronic effects contribute to thermal energy storage capacity.

The entropy values (S), measured in cal mol^{-1} K^{-1}, reveal equally fascinating trends in system disorder and molecular freedom. The isolated molecules show a clear progression: H_2 (31.139) < N_2 (45.722) < O_2 (46.757) < CO (47.183) < NO (48.996) < CO_2 (50.983) < SO_2 (59.204) < Al_8O_{12} (144.385). Upon adsorption, all complexes exhibit markedly higher entropy values: H_2@Al_8O_{12}_1 (154.095) < SO_2@Al_8O_{12}_2 (162.819) < CO@Al_8O_{12}_17 (160.867) < N_2@Al_8O_{12}_3 (161.115) < O_2@Al_8O_{12}_2 (164.068) < CO_2@Al_8O_{12}_9 (165.67) < NO@Al_8O_{12}_9 (165.521) < NO_2@Al_8O_{12}_13 (171.104). This entropy enhancement can be rationalized through several mechanisms: (1) increased configurational entropy due to multiple possible adsorption sites on the Al_8O_{12} surface, (2) coupling between adsorbate and substrate vibrational modes creating new quantum states, (3) modified rotational states of the adsorbed molecules, and (4) electronic state mixing between adsorbate and substrate. The observation that NO_2@Al_8O_{12}_13 exhibits the highest entropy (171.104) despite surface confinement suggests that the system compensates for the loss of translational freedom through enhanced vibrational and rotational contributions.

The binding energies (BE) in hartree units provide crucial insights into the strength and nature of adsorbate-substrate interactions: SO_2 (−0.0472) > CO (−0.0246) > CO_2 (−0.0213) > NO_2 (−0.0211) > O_2 (−0.0192) > NO (−0.0179) > N_2 (−0.0159) > H_2 (−0.0088). This trend reveals several important features of the interaction mechanism: (1) molecules with higher electron-accepting capability (SO_2, CO_2) show stronger binding due to enhanced orbital interactions, (2) polar molecules generally exhibit stronger binding than non-polar ones due to electrostatic contributions, (3) molecular size alone does not determine binding strength, as evidenced by the relatively weak binding of H_2 despite its optimal fit in substrate pores, and (4) the presence of electron-withdrawing groups enhances binding through increased electron density transfer between adsorbate and substrate.

3.2. Conceptual DFT

In conceptual density functional theory (CDFT),[58,59] the primary focus is on understanding the global reactivity and chemical properties of molecules by examining the energies of the Highest Occupied Molecular Orbital (HOMO) and the Lowest Unoccupied Molecular Orbital (LUMO).[60] These energies are determined using molecular orbital theory, which describes the electronic energy levels of the highest occupied and lowest unoccupied orbitals. Electronegativity (χ), a measure of an atom or molecule's ability to attract electrons in a chemical bond, can be mathematically related to the HOMO and LUMO energies through the following equation:

$$\chi = \frac{1}{2}(\varepsilon_{\text{HOMO}} + \varepsilon_{\text{LUMO}}) \tag{3}$$

Electronegativity affords profound insights into the essence of chemical bonding, the molecular polarity, and the overall reactivity of compounds. In CDFT, the chemical potential (μ) elucidates the energy variation arising from the addition or removal of an electron while holding the external potential constant. This quantity can be articulated in relation to the HOMO energy of the molecule ($\mu = -\varepsilon_{\text{HOMO}}$).[61–64] The presence of the negative sign signifies that the inclusion of an electron results in an energy decrease, owing to the negatively charged nature of electrons. Hardness (η), as a descriptor, serves to quantify the molecular resistance to electron transfer and can be computed based on the energy difference between the LUMO and HOMO orbitals.

$$\eta = \varepsilon_{\text{LUMO}} - \varepsilon_{\text{HOMO}} \tag{4}$$

Higher hardness values indicate that the molecule requires a higher energy input to transfer an electron, making it less reactive. Softness (S) is the reciprocal of hardness and is related to the polarizability and chemical reactivity of the system. It can be calculated using the hardness ($S = 1/\eta$). Softness values reflect the ease of electron transfer, with higher softness indicating greater reactivity and electron affinity. The electrophilicity index (ω) combines information from the chemical potential (μ) and the global hardness (η) of the system. It is used to predict the tendency of a molecule to accept electrons in chemical reactions and is given by the following formula,[65–67]

$$\omega = \frac{\mu^2}{2\eta} \tag{5}$$

A higher electrophilicity index suggests a greater ability of the molecule to act as an electron acceptor in chemical reactions. In Table 2, we present the quantitative values of the

Table 2 The values of HOMO energy (ε_{HOMO}), LUMO energy (ε_{LUMO}), HOMO–LUMO energy gap (HLG), chemical hardness (η), chemical potential (μ), and electrophilicity index (ω). All values are in eV obtained at ωB97XD/Def2-TZVP level of theory

Systems	ε_{HOMO}	ε_{LUMO}	HLG	η	μ	ω
Al_8O_{12}	−9.7145	−0.9856	8.7289	4.3644	−5.3500	1.6396
CO	−12.7597	1.2795	14.0392	7.0196	−5.7401	1.1735
CO_2	−12.5904	2.7513	15.3418	7.6709	−4.9195	0.7888
H_2	−14.0550	4.5239	18.5789	9.2894	−4.7655	0.6112
N_2	−14.2389	1.5097	15.7486	7.8743	−6.3646	1.2861
NO	−8.1536	−0.7309	7.4227	3.7114	−4.4423	1.3293
NO_2	−10.1488	−0.4299	9.7188	4.8594	−5.2894	1.4393
O_2	−9.2345	−2.7818	6.4526	3.2263	−6.0081	2.7971
SO_2	−11.4650	−1.6411	9.8239	4.9119	−6.5530	2.1856
$CO@Al_8O_{12}\_17$	−9.4818	−0.7080	8.7738	4.3869	−5.0949	1.4793
$CO_2@Al_8O_{12}\_9$	−9.4979	−0.7358	8.7621	4.3810	−5.1168	1.4941
$H_2@Al_8O_{12}\_1$	−9.6024	−0.8221	8.7803	4.3902	−5.2122	1.5470
$N_2@Al_8O_{12}\_3$	−9.5153	−0.7453	8.7700	4.3850	−5.1303	1.5006
$NO@Al_8O_{12}\_9$	−9.5180	−2.3674	7.1506	3.5753	−5.9427	2.4694
$NO_2@Al_8O_{12}\_13$	−9.4483	−1.8792	7.5691	3.7846	−5.6638	2.1190
$O_2@Al_8O_{12}\_2$	−9.5387	−4.4866	5.0521	2.5260	−7.0126	4.8670
$SO_2@Al_8O_{12}\_2$	−9.9286	−1.0615	8.8671	4.4336	−5.4951	1.7027

descriptors calculated from the HOMO and LUMO energies obtained through SCF calculations. Additionally, for all the studied configurations, Table S2 is provided in the ESI,† containing all the values from the conceptual density functional theory analyses. Analyzing isolated molecular systems reveals that frontier orbital energies, specifically HOMO and LUMO energies, follow distinct patterns. These orbital energy levels indicate the molecular stability and electron-donating or accepting abilities of various gases and pollutants like H_2, N_2, CO, CO_2, SO_2, NO_2, O_2, and NO. Notably, HOMO values show a trend from H_2 with the lowest (−14.0550 eV) to Al_8O_{12} with the highest values (−9.7145 eV), reflecting increased stability among diatomic gases with covalent bonds (*e.g.*, H_2 and N_2) and a decrease in stability among molecules with unpaired electrons or weaker bonding (*e.g.*, O_2, NO). LUMO energy trends present a different sequence: with O_2, NO, and NO_2 having the lowest values and CO_2 and H_2 the highest, the observed trend aligns with the electron-accepting tendencies of each molecule. Lower LUMO energies generally correspond to molecules with high electronegativity and electron-accepting abilities, indicative of their reactivity when acting as electron acceptors in potential catalytic or reactive environments.

The HOMO–LUMO gap, which directly correlates with molecular stability and reactivity, provides further insights into the potential of these molecules to interact with Al_8O_{12} upon complexation. This gap follows a sequence from O_2 (6.4526 eV), with the smallest gap indicative of high reactivity, to H_2 (18.5789 eV), with the largest gap reflective of significant stability. Such variations align with bond types, including single, double, or triple bonds, affecting the electronic structure and stability. The stability of molecules such as N_2, characterized by a triple bond, contrasts with molecules like O_2 and NO, which are more reactive due to their smaller HOMO–LUMO gaps and the presence of unpaired electrons. Chemical hardness, which is directly proportional to the HOMO–LUMO gap, supports this trend, underscoring the electron cloud deformation resistance of stable molecules like H_2 and N_2 compared to the reactive nature of molecules such as NO and O_2. Chemical potential values add further nuance by indicating electron mobility and retention tendencies, where more negative values represent stronger electron retention, as seen in SO_2 and O_2. Consequently, molecules such as NO, with a less negative chemical potential, exhibit a greater propensity for electron exchange, which directly impacts reactivity potential. Fig. 6 illustrates the total density of states (TDOS) and aims to demonstrate the changes in the electronic density of the aluminum oxide cluster molecule both in isolation and after interaction with various gases. As observed, these changes are relatively minor. For better reference, each gas is depicted in the figure to show how it affects the electronic densities, highlighting the subtle variations induced by the presence of different gaseous species.

Complexation with Al_8O_{12} significantly modifies these electronic characteristics, marking shifts in reactivity, molecular stability, and binding energies. Upon interacting with Al_8O_{12}, HOMO energies across complexes cluster within a narrower range of approximately −9.4 to −9.9 eV, indicating a significant destabilization effect, especially for previously stable molecules such as H_2 and N_2. This clustering effect reflects electronic level alignment, likely resulting from electron density redistribution between the molecules and the Al_8O_{12} cage. The observed shift in LUMO energies ranges from −4.4866 eV ($O_2@Al_8O_{12}\_2$) to −0.7080 eV ($CO@Al_8O_{12}\_17$), where molecules like H_2 and CO_2 exhibit marked stabilization effects. The spread in LUMO values suggests that the Al_8O_{12} complexation alters the electron-accepting potential, creating a stable yet reactive molecular environment conducive to further interactions. Consequently, the HOMO–LUMO gap in complexes consistently decreases, suggesting increased reactivity potential. The $O_2@Al_8O_{12}$ complex maintains the smallest HOMO–LUMO gap (5.0521 eV), preserving its reactive potential, while traditionally stable molecules, such as H_2 and N_2, exhibit enhanced reactivity potential due to significant gap reductions, thus demonstrating

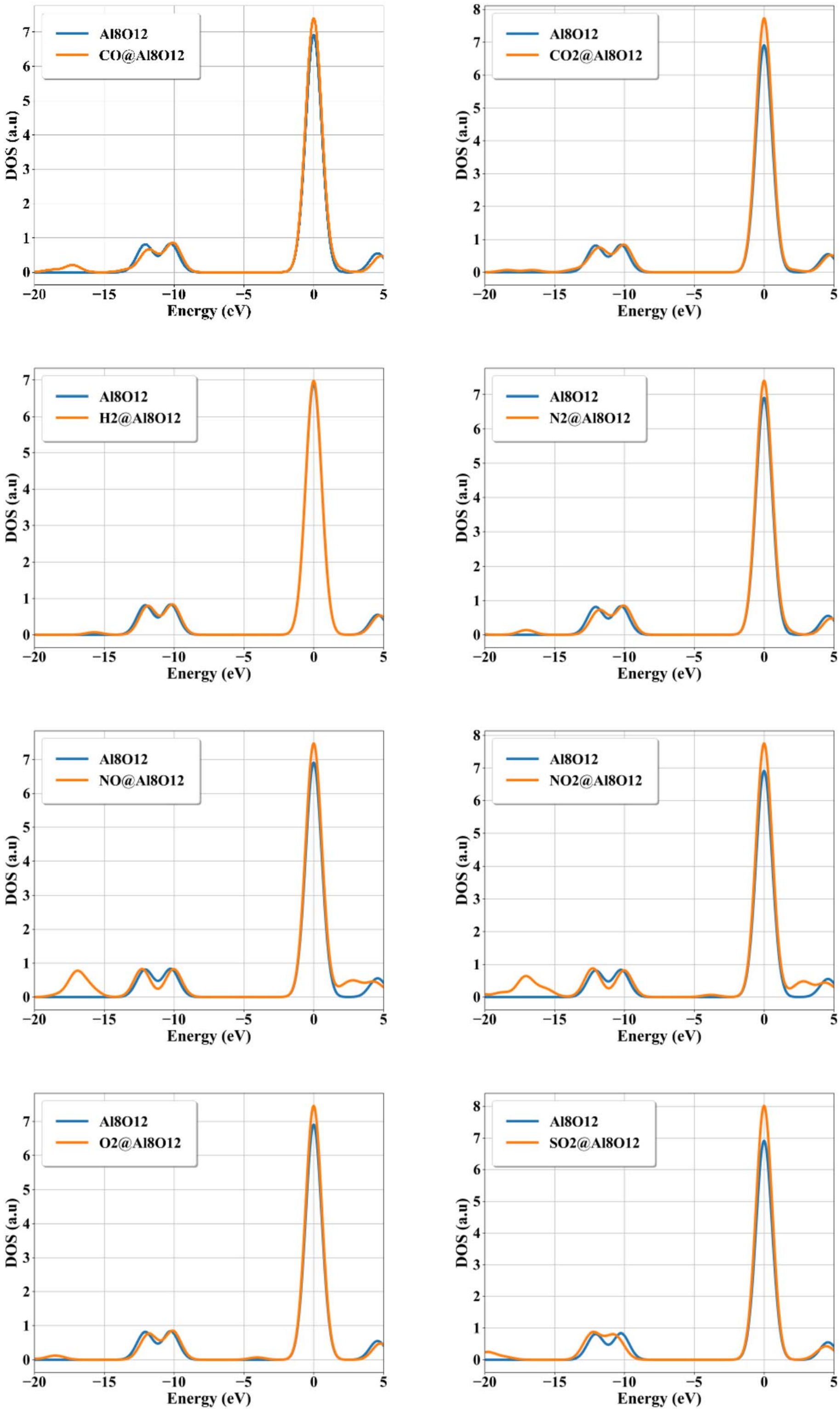

Fig. 6 Total Density of States (TDOS) plot for the Al_8O_{12} cluster and the adsorbed gases, including CO, CO_2, H_2, N_2, NO, NO_2, O_2, and SO_2. The *x*-axis represents the energy levels (in eV), while the *y*-axis shows the total number of electronic states per energy interval (states per eV). The calculations are performed at ωB97XD/Def2-TZVP level of theory.

Al_8O_{12}'s capacity to adjust molecular electronic characteristics systematically.

The electrophilicity index for these complexes also reflects enhanced electron-accepting capacity post-complexation, with values generally surpassing those of the isolated molecules. Notably, $O_2@Al_8O_{12}\_2$ shows the highest electrophilicity value (4.8670), suggesting substantial enhancement in electron-accepting behavior upon adsorption. This increase in electrophilicity across complexes implies that Al_8O_{12} could effectively serve as a catalyst or electronic mediator, enhancing the reactivity of adsorbed molecules for applications requiring activation of inert gases. Binding energy trends, especially among diatomic molecules, demonstrate consistent patterns based on molecular structure: molecules with greater electron density or molecular polarity (*e.g.*, O_2, NO) show more robust binding interactions with Al_8O_{12}, while more inert molecules like N_2 exhibit weaker binding. Complex triatomic molecules such as CO_2, NO_2, and SO_2 demonstrate variable binding energies due to their unique geometries and available binding sites, enabling multiple coordination modes. These findings suggest that the Al_8O_{12} cage could modulate binding strength and electronic behavior based on the molecular geometry and electron distribution of the adsorbed species.

The electronic reconfiguration facilitated by Al_8O_{12} has direct implications for catalytic applications, gas adsorption, and sensing technologies. Al_8O_{12}'s role as an electronic modifier is exemplified by consistent HOMO–LUMO gap reduction, increased electrophilicity, and uniform HOMO energy alignment among complexes. These modifications suggest that Al_8O_{12} could stabilize adsorbed molecules while enhancing their reactive potential, making it an attractive candidate for catalytic systems targeting gas activation or selective molecular transformations. The elevated electrophilicity index of $O_2@Al_8O_{12}$, in particular, signifies potential applications in oxidation catalysis or as a component in fuel cell technology, where O_2 activation is crucial. The trends observed with Al_8O_{12} also underscore the cage's capacity to selectively bind and activate stable molecules, expanding its utility in systems requiring precise molecular reactivity modulation. In sum, Al_8O_{12}'s systematic influence over molecular electronic properties offers substantial potential for applied chemistry, particularly within catalysis, where it could enable selective reactivity and conversion processes.

From an examination of the energy of HOMO and LUMO orbitals, emerges a distinct subject of interest—the investigation of energy gap variations during the surface adsorption process. As demonstrated in Table 2, the energy gap for the Al_8O_{12} cluster stands at approximately 8.72 eV in its isolated state. However, following the adsorption of gases, this value undergoes a profound reduction. Notably, the most significant decrease occurs with O_2 gas, leading to a decline of up to 5.05 eV, while for NO, this reduction amounts to 7.15 eV. This remarkable property can be harnessed in the development of highly responsive gas sensors. It becomes evident that in the presence of a mixture of gases, the sensor exhibits heightened sensitivity to O_2. To assess this sensitivity effectively, one may compare the electrical conductivity of the absorber, thereby determining the sensor's response and recovery times, which can be derived from the following equations,[68]

$$S = \left|\left(\frac{\sigma_1}{\sigma_2}\right) - 1\right| = \exp\left(\frac{|\Delta \mathrm{HLG}|}{k_\mathrm{b}T}\right) - 1 \tag{6}$$

$$\sigma = AT^{3/2}e^{\frac{\mathrm{HLG}}{2k_\mathrm{b}T}} \tag{7}$$

$$\tau = \nu^{-1}\exp\left(\frac{|E_\mathrm{b}|}{k_\mathrm{b}T}\right) \tag{8}$$

In the given context, where ν represents the frequency of bond rupture attempts and is assumed to be 1 terahertz (THz), and E_b signifies the binding energy between the gas and the cluster. In eqn (7), (A) represents a coefficient that may be disregarded, as evident in direct proportionality within eqn (6). Electrical conductivity is denoted by the symbol σ, while temperature and the Boltzmann constant are respectively represented by k_b and T. Based on the aforementioned relationships, it is evident that the absorbent sensor exhibits remarkable efficacy, yielding a rapid recovery rate, which is highly coveted. As a consequence, the suggested sensor can promptly regenerate and be employed iteratively within the same environment.

3.3. NBO analysis

NBO analysis, utilizing methods like Mulliken, Mayer, and Wiberg bond indices (WBI), offers insights into electron distribution, bond strength, and delocalization effects in molecular systems. The Fuzzy Bond Order (FBO) and Laplacian Bond Order (LBO) methods, introduced by Mayer and Lu respectively, further refine bond character analysis by emphasizing stability across basis sets and electron density concentration in bonding regions. These bond order methods, summarized in Table 3, reveal key bonding trends in the interactions between various gases (*e.g.*, CO, CO_2, H_2, N_2, NO, NO_2, O_2, SO_2) and the Al_8O_{12} cluster.

Mulliken bond order values vary significantly among the bonds, with most values being close to zero or even negative, indicating weak or antibonding interactions between the gas molecules and the Al_8O_{12} cluster. The MBO for CO with Al (0.0408) is low, suggesting a minimal bonding interaction, while for CO_2, H_2, NO, and NO_2, the bond orders are negative, indicating antibonding character. For instance, the NO⋯Al interaction shows the most negative Mulliken bond order (−0.7154), highlighting a strong antibonding effect between NO and the Al center. The SO_2⋯O and O⋯Al interactions are slightly positive (0.0777 and 0.1789, respectively), suggesting mild bonding, although the interaction is still weak. Mayer bond order values are generally more positive than Mulliken

Table 3 The values of bond order analyses including Mulliken bond order, Mayer bond order, WBO, FBO, and LBO between the specified atoms in gases (left atom) and Al_8O_{12} atom (right atom) obtained at ωB97XD/Def2TZVP level of theory

System	Bond	Mulliken	Mayer	WBI	FBO	LBO
$CO@Al_8O_{12}$_17	C⋯Al	0.0408	0.4026	0.5640	0.6370	0.4439
$CO_2@Al_8O_{12}$_9	O⋯Al	−0.5971	−0.3319	0.1695	0.4705	0.0530
$H_2@Al_8O_{12}$_1	H⋯Al	−0.1696	−0.1069	0.0545	0.1429	0.0119
$N_2@Al_8O_{12}$_3	N⋯Al	0.2204	0.4181	0.4144	0.4962	0.1012
$NO@Al_8O_{12}$_9	N⋯Al	−0.7154	−0.4385	0.1183	0.3334	0.1165
$NO_2@Al_8O_{12}$_13	O⋯Al	−0.5520	−0.3674	0.1616	0.4396	0.0530
$O_2@Al_8O_{12}$_2	O⋯Al	0.0364	0.1212	0.3857	0.5156	0.0550
$SO_2@Al_8O_{12}$_2	S⋯O	0.0777	0.0918	0.0269	0.0425	0.0000
	O⋯Al	0.1789	0.4628	0.7463	0.8649	0.0946

bond orders, demonstrating the versatility of this metric for quantifying bonding interactions. The bond order values for systems like CO⋯Al (0.4026) and N_2⋯Al (0.4181) are significantly higher than in Mulliken bond analysis, indicating a moderate bonding interaction. However, for NO⋯Al and NO_2⋯Al, the Mayer bond order is negative, similar to the Mulliken bond order, but less intense. This pattern suggests that Mayer bond orders are more stable and generally closer to the empirical understanding of bonding, particularly in polar interactions, where Mayer bond orders are less sensitive to basis sets than other methods. The WBI reveals a pattern consistent with Mayer bond orders, especially in nonpolar interactions. For instance, the bond order between CO and Al is 0.5640, and for N_2 and Al, it is 0.4144, suggesting moderate bonding, aligning closely with Mayer bond order values. However, the WBI tends to be lower for polar bonds, as seen in the negative values for NO⋯Al and NO_2⋯Al, indicating that this index may overestimate bonding in some cases. The SO_2⋯O and O_2⋯Al interactions are also close to the Mayer bond order values, indicating that WBI is generally aligned with Mayer bond orders in low-polarity cases but diverges slightly in systems with higher polarity or antibonding characteristics. FBO values for the systems studied tend to be higher than WBI and Mayer bond order values, especially in cases where the electron density distribution is significant in the bonding region. For instance, FBO is notably high for CO⋯Al (0.6370) and O_2⋯Al (0.5156), reflecting significant bonding interactions due to electron density overlap in these regions. The FBO for SO_2⋯Al (0.8649) is the highest among all bond order methods, suggesting that FBO may exaggerate bonding interactions for such polar bonds due to the fuzzy space definition, capturing a broader electron density. This increased bond order in FBO analysis for O_2, CO, and SO_2 is consistent with fuzzy atomic spaces being less sensitive to basis sets, thus stabilizing bond order values across computational levels. The LBO values are generally lower across the board, with most values under 0.5, showing that this method is particularly suited for capturing covalent interactions rather than weak polar interactions. The CO⋯Al bond exhibits a moderate LBO value of 0.4439, indicating covalent character, while bonds like N_2⋯Al and O_2⋯Al show lower values (0.1012 and 0.0550, respectively), suggesting weak interactions. The LBO for SO_2⋯Al (0.0946) is lower than FBO and WBI, consistent with LBO's design to capture localized electron density concentrations typical of covalent bonding. Overall, FBO and WBI tend to indicate higher bond orders for nonpolar bonds and polar bonds with significant electron density overlap, whereas LBO captures covalent interactions more effectively. Mayer bond order generally shows a stable middle-ground estimation for bond strength, and the Mulliken bond order analysis highlights antibonding interactions in some systems. The trends show that while FBO may overestimate polar interactions, LBO remains consistent for covalent interactions, and Mayer bond orders appear less dependent on basis set variations, aligning closely with empirical bonding expectations. This comparative analysis allows for a robust interpretation of bonding trends, especially in complex systems like metal oxide clusters with interacting gaseous species.

Natural atomic charges and electron configurations derived from NBO analysis provide fundamental insights into the electronic structure and bonding characteristics of molecular systems. The analysis transforms the molecular wavefunction into localized orbitals that correspond to an optimally compact Lewis structure-like description of the electron density distribution, offering chemically intuitive interpretations of electronic properties. Natural charges, obtained through NBO population analysis, represent a more robust alternative to traditional Mulliken charges. These charges are calculated by subtracting the sum of natural atomic orbital (NAO) populations from the nuclear charge of each atom. Unlike Mulliken charges, natural charges show remarkable stability with respect to basis set variations, making them more reliable for comparing electronic distributions across different computational methods. For instance, in polar covalent bonds, the more electronegative atom typically exhibits a negative natural charge, while the less electronegative partner shows a positive charge. The magnitude of these charges provides direct insight into the ionic character of bonds and the degree of electron transfer between atoms. The natural electron configuration analysis reveals the population of different atomic orbitals (s, p, d, f) in the molecular environment, offering detailed information about hybridization and bonding patterns. This analysis presents the electron occupation in terms of atomic-like orbitals, making it straightforward to identify deviations from typical atomic ground state configurations. For example, in transition metal complexes, the natural electron configuration can reveal the extent of d-orbital participation in bonding and the degree of electron transfer between metal and ligands. The analysis might show configurations like [core]4s(0.82)3d(8.45) 4p(0.52), where the decimal numbers indicate orbital populations, revealing partial electron transfer and orbital hybridization. The values obtained from the aforementioned analyses are listed in Table 4 and are further explained below.

In isolated CO, the natural charges on carbon and oxygen atoms are 0.49885 and −0.49885, respectively, signifying charge polarization with electron density skewed toward oxygen. Carbon's electron configuration, [core]2s(1.66)2p(1.79), indicates partially filled 2p orbitals, with minor contributions in 3s and 3p. Upon CO's adsorption onto Al_8O_{12}, the natural charge on carbon increases to 0.58854, while oxygen's negative charge reduces to −0.39389, highlighting charge transfer predominantly toward the Al_8O_{12} surface. This adjustment in charge and increased electron density in carbon's 2p orbital suggests strengthened covalent interactions between carbon and the Al atoms. The overall increase in covalent character reflects electron redistribution mechanisms that stabilize CO adsorption by balancing electron density around the interaction site. For isolated CO_2, the carbon atom has a notable positive charge of 1.04427, with the oxygens symmetrically charged at −0.52213 each, which is consistent with the electron-withdrawing behavior of oxygen in a linear CO_2 structure. Carbon's electron configuration, [core]2s(0.67)2p(2.24), reflects significant depletion in the 2s orbital, aligning with its electron donor role. Upon adsorption on Al_8O_{12}, carbon's charge further increases to 1.13686, and the symmetry in oxygen charges breaks (−0.43023

Table 4 Values of natural charge and electron configurations for specified gas-phase atoms in both isolated and gas/cluster systems. The observed variations in natural charge and electron configurations provide insights into the charge transfer mechanisms occurring during interactions between gas atoms and the cluster, reflecting the underlying electronic dynamics and bonding characteristics. All calculations are performed at ωB97XD/Def2-TZVP level of theory

Systems	Atom	Natural charge	Natural electron configuration
CO	C	0.49885	[Core]2s(1.66)2p(1.79)3s(0.02)3p(0.01)3d(0.01)
	O	−0.49885	[Core]2s(1.73)2p(4.75)3s(0.01)3d(0.01)
$CO@Al_8O_{12}$_17	C	0.58854	[Core]2s(1.43)2p(1.93)3s(0.02)3p(0.02)3d(0.01)
	O	−0.39389	[Core]2s(1.71)2p(4.66)3s(0.01)3d(0.02)
CO_2	C	1.04427	[Core]2s(0.67)2p(2.24)3p(0.03)3d(0.02)
	O	−0.52213	[Core]2s(1.72)2p(4.79)3d(0.01)
	O	−0.52213	[Core]2s(1.72)2p(4.79)3d(0.01)
$CO_2@Al_8O_{12}$_9	C	1.13686	[Core]2s(0.65)2p(2.17)3p(0.02)3d(0.02)
	O	−0.43023	[Core]2s(1.71)2p(4.70)3d(0.01)
	O	−0.61427	[Core]2s(1.68)2p(4.91)3p(0.01)3d(0.01)
H_2	H	0	1s(1.00)
	H	0	1s(1.00)
$H_2@Al_8O_{12}$_1	H	0.0307	1s(0.97)
	H	0.03919	1s(0.96)
N_2	N	0	[Core]2s(1.61)2p(3.35)3s(0.02)3p(0.01)3d(0.01)
	N	0	[Core]2s(1.61)2p(3.35)3s(0.02)3p(0.01)3d(0.01)
$N_2@Al_8O_{12}$_3	N	−0.04804	[Core]2s(1.50)2p(3.49)3s(0.03)3p(0.02)
	N	0.15965	[Core]2s(1.59)2p(3.21)3s(0.02)3p(0.01)3d(0.02)
NO	N	0.1877	[Core]2s(1.70)2p(3.06)3s(0.03)3p(0.02)3d(0.01)
	O	−0.1877	[Core]2s(1.72)2p(4.44)3s(0.01)3p(0.01)3d(0.01)
$NO@Al_8O_{12}$_9	N	0.18397	[Core]2s(1.60)2p(3.16)3s(0.02)3p(0.03)3d(0.01)
	O	−0.05619	[Core]2s(1.71)2p(4.32)3s(0.01)3p(0.01)3d(0.01)
NO_2	N	0.5297	[Core]2s(1.19)2p(3.21)3s(0.03)3p(0.03)3d(0.02)
	O	−0.26485	[Core]2s(1.74)2p(4.51)3p(0.01)3d(0.01)
	O	−0.26485	[Core]2s(1.74)2p(4.51)3p(0.01)3d(0.01)
$NO_2@Al_8O_{12}$_13	N	0.61164	[Core]2s(1.18)2p(3.14)3s(0.02)3p(0.02)3d(0.02)
	O	−0.14117	[Core]2s(1.73)2p(4.40)3s(0.01)3p(0.01)3d(0.01)
	O	−0.36485	[Core]2s(1.71)2p(4.63)3p(0.01)3d(0.01)
O_2	O	0	[Core]2s(1.79)2p(4.18)3s(0.01)3p(0.01)3d(0.01)
	O	0	[Core]2s(1.79)2p(4.18)3s(0.01)3p(0.01)3d(0.01)
$O_2@Al_8O_{12}$_2	O	0.1257	[Core]2s(1.78)2p(4.07)3s(0.01)3p(0.01)3d(0.01)
	O	−0.0223	[Core]2s(1.74)2p(4.24)3s(0.01)3p(0.01)3d(0.01)
SO_2	S	1.57978	[Core]3s(1.62)3p(2.60)4s(0.05)3d(0.13)4p(0.02)
	O	−0.78989	[Core]2s(1.82)2p(4.96)3d(0.01)
	O	−0.78989	[Core]2s(1.82)2p(4.96)3d(0.01)
$SO_2@Al_8O_{12}$_2	S	1.76782	[Core]3s(1.54)3p(2.53)4s(0.03)3d(0.11)4p(0.03)
	O	−0.85216	[Core]2s(1.81)2p(5.03)3d(0.01)
	O	−1.05774	[Core]2s(1.78)2p(5.26)3d(0.01)

and −0.61427), showing one oxygen interacting more strongly with Al_8O_{12}. This asymmetry suggests partial electron transfer to the Al atoms, with carbon retaining a higher positive charge, enhancing the electrostatic stabilization of the adsorption complex. In free H_2, both hydrogen atoms remain neutral with full 1s occupancy, demonstrating the covalent bond stability. After H_2 adsorbs onto Al_8O_{12}, each hydrogen becomes slightly positively charged (0.0307 and 0.03919), suggesting weak electron transfer toward the Al_8O_{12} surface. The small decrease in the 1s orbital occupancy (0.97 and 0.96) indicates minor charge redistribution, consistent with physisorption rather than chemisorption. This slight polarization without significant electron sharing confirms that H_2 adsorbs weakly on the Al_8O_{12} surface, driven primarily by van der Waals forces. In the free N_2 molecule, both nitrogen atoms are neutral with an electron configuration [core]2s(1.61)2p(3.35), reflecting a stable triple bond with no charge transfer. Upon adsorption, one nitrogen gains a slight negative charge (−0.04804), while the other becomes positively charged (0.15965), indicating charge polarization due to interaction with Al_8O_{12}. This polarization likely results from asymmetric interaction where one nitrogen atom donates electron density to Al. The small increase in the 2p occupancy of the negatively charged nitrogen suggests weak interaction, aligning with adsorption through dipole interaction rather than covalent bonding. In free NO, nitrogen has a positive charge of 0.1877, with oxygen bearing a corresponding negative charge (−0.1877), indicative of electron sharing with nitrogen slightly electron-deficient. Upon adsorption on Al_8O_{12}, nitrogen's charge marginally decreases (0.18397), while oxygen's negative charge is reduced to −0.05619, indicating electron redistribution toward Al atoms. This minor reduction in nitrogen's 2p occupancy, with slight increases in 3p and 3d orbital occupancy, suggests weak chemisorption, where nitrogen experiences weak polarization to balance electrostatic interactions with Al atoms. The free NO_2 molecule exhibits a substantial positive charge on nitrogen (0.5297) and negative charges on both oxygens (−0.26485 each), indicative of strong electron-withdrawing behavior from nitrogen. Upon adsorption, nitrogen's charge increases to 0.61164, while the oxygen charges become asymmetric (−0.14117 and −0.36485), suggesting one oxygen interacts more closely with Al_8O_{12}. This asymmetry likely enhances stability by facilitating electron redistribution that favors electrostatic interactions, with nitrogen retaining high positive character to stabilize binding with the Al_8O_{12} surface. In free O_2, both oxygen atoms are neutral with electron configurations of [core]2s(1.79)2p(4.18), reflective of a stable double bond. Upon adsorption, one oxygen acquires a slight positive charge (0.1257) while the other becomes slightly negative (−0.0223), suggesting minor charge redistribution toward Al_8O_{12}. The minimal shift in 2p occupancy indicates weak physisorption rather than chemisorption, with the slight polarization enhancing stability through dipole interaction between the O_2 molecule and the Al_8O_{12} surface. For isolated SO_2, sulfur carries a significant positive charge (1.57978), while each oxygen atom has a negative charge of −0.78989, which demonstrates electron withdrawal by the oxygen atoms. After adsorption onto Al_8O_{12}, sulfur's charge increases to 1.76782, while oxygen charges become more negative (−0.85216 and −1.05774), indicating strong polarization due to interaction with Al atoms. The electron redistribution, particularly enhanced oxygen 2p and 3d orbital occupancy, suggests stronger chemisorption driven by sulfur and oxygen electron donation toward the Al atoms in Al_8O_{12}, consistent with the formation of a stable, highly polarized adsorption complex.

Carbon monoxide (CO) exhibits notable electronic redistribution upon adsorption on Al_8O_{12}_17. The natural charge of the C atom increases from +0.499 to +0.589, while the O atom's negative charge decreases from −0.499 to −0.394. This charge redistribution is reflected in the electron configuration, where the C 2p occupancy increases from 1.79 to 1.93, while the O 2p occupancy decreases from 4.75 to 4.66, indicating a weakening of the CO triple bond and enhanced interaction with the substrate. For CO_2, adsorption on Al_8O_{12}_9 leads to asymmetric charge distribution between the two oxygen atoms. The carbon atom becomes more positively charged (from +1.044 to +1.137), while one oxygen atom becomes less negative (−0.522 to −0.430) and the other more negative (−0.522 to −0.614). This asymmetric charge distribution suggests chemisorption with possible geometric distortion from the linear CO_2 structure, supported by changes in the O 2p orbital occupancies (4.79 to 4.70 and 4.91, respectively). The H_2 molecule, initially having neutral atoms with 1s(1.00) configurations, undergoes minor charge transfer upon adsorption at Al_8O_{12}_1. Both hydrogen atoms acquire slight positive charges (+0.031 and +0.039), with corresponding decreases in 1s orbital occupancies to 0.97 and 0.96, indicating weak physisorption with minimal electronic structure perturbation. Molecular nitrogen (N_2) shows interesting charge redistribution upon adsorption at Al_8O_{12}_3. The initially equivalent N atoms (charge = 0) become inequivalent, with one acquiring a negative charge (−0.048) and the other a positive charge (+0.160). This is accompanied by significant changes in the 2p orbital occupancies (from 3.35 to 3.49 and 3.21, respectively), suggesting end-on chemisorption with substantial electron density redistribution. The NO molecule demonstrates modified charge distribution after adsorption on Al_8O_{12}_9. While the nitrogen atom maintains a similar positive charge (+0.188 *vs.* +0.184), the oxygen atom becomes significantly less negative (−0.188 to −0.056). The O 2p orbital occupancy decreases from 4.44 to 4.32, while the N 2p occupancy increases from 3.06 to 3.16, indicating electronic reorganization that may affect the N–O bond strength. For NO_2, adsorption on Al_8O_{12}_13 results in asymmetric charge distribution between oxygen atoms. The nitrogen becomes more positive (from +0.530 to +0.612), while one oxygen becomes less negative (−0.265 to −0.141) and the other more negative (−0.265 to −0.365). This charge redistribution, coupled with changes in 2p orbital occupancies, suggests strong chemisorption with possible structural deformation. The O_2 molecule transitions from equivalent atoms (charge = 0) to inequivalent atoms upon adsorption at Al_8O_{12}_2, with charges of +0.126 and −0.022. The 2p orbital occupancies change from 4.18 to 4.07 and 4.24, respectively, indicating significant electron density redistribution and possible activation of the O–O bond. SO_2 undergoes substantial electronic reorganization when adsorbed on Al_8O_{12}_2. The sulfur atom becomes more positive (from +1.580 to +1.768), while the oxygen atoms show different degrees of negative charge (−0.790 to −0.852 and −1.058). The asymmetric charge distribution on oxygen atoms, coupled with changes in orbital occupancies, suggests strong chemisorption with possible geometric distortion from the original SO_2 structure.

3.4. QTAIM analysis

QTAIM provides valuable insights into the electron density distribution within molecular systems, allowing for the classification of bond types such as covalent, ionic, and van der Waals interactions. By analyzing descriptors like Lagrangian kinetic energy ($G(r)$) and potential energy density ($V(r)$), QTAIM enables the classification of interactions and provides predictive power regarding chemical reactivity. The results from this analysis, summarized in Table 5 and illustrated in Fig. 7 and 8, reveal the critical bonding points and offer a deeper understanding of the interactions between gas molecules and the aluminum oxide cluster.

The CO_Al_8O_{12}_17 system exhibits a closed-shell interaction, as evidenced by the positive Laplacian of electron density ($\nabla^2\rho(\mathbf{r})$) value of 0.1230 and the relatively low electron localization function (ELF) value of 0.0886 at the bond critical point (BCP). A closed-shell interaction is characterized by a depletion of electron density at the BCP, indicating a lack of significant electron sharing between the interacting atoms. This type of interaction is typically observed in ionic bonds, where electrostatic forces dominate, or in van der Waals interactions, where weak intermolecular forces are at play. The positive total energy density ($H(\mathbf{r})$) value of −0.0174 further suggests a slightly destabilizing interaction, consistent with a weak interaction such as a van der Waals interaction. These findings collectively

Table 5 Different QTAIM parameters at BCP (3, −1) between gases and clusters (CP number) including electron density $\rho(\mathbf{r})$, Laplacian of electron density $\nabla^2\rho(\mathbf{r})$, Lagrangian kinetic energy $G(\mathbf{r})$, total energy density $H(\mathbf{r})$, potential energy density $V(\mathbf{r})$, $G(\mathbf{r})/V(\mathbf{r})$ ratio, ellipticity of electron density (ε), and eta index (η) obtained at ωB97XD/Def2TZVP level of theory

Systems	CP	$\rho(\mathbf{r})$	$G(\mathbf{r})$	$V(\mathbf{r})$	$H(\mathbf{r})$	$\nabla^2\rho(\mathbf{r})$	ELF	LOL	ε	η	$G(\mathbf{r})/V(\mathbf{r})$
$\mathrm{CO\_Al_8O_{12}\_17}$	40	0.0428	0.0481	−0.0655	−0.0174	0.1230	0.0886	0.2377	0.2995	0.3124	0.7346
$\mathrm{CO_2\_Al_8O_{12}\_9}$	36	0.0178	0.0521	−0.0380	0.0141	0.2646	0.0045	0.0629	0.4623	0.0945	1.3701
	45	0.0176	0.0198	−0.0219	−0.0021	0.0708	0.0292	0.1478	0.1394	0.1758	0.9044
$\mathrm{H_2\_Al_8O_{12}\_1}$	30	0.0063	0.0085	−0.0074	0.0011	0.0383	0.0052	0.0675	0.4843	0.1554	1.1445
	35	0.0063	0.0085	−0.0074	0.0011	0.0382	0.0052	0.0673	0.4914	0.1554	1.1457
$\mathrm{N_2\_Al_8O_{12}\_3}$	41	0.0279	0.0352	−0.0413	−0.0061	0.1166	0.0419	0.1730	0.0119	0.2282	0.8532
$\mathrm{NO\_Al_8O_{12}\_9}$	39	0.0044	0.0075	−0.0074	0.0002	0.0310	0.0022	0.0444	0.1084	0.1030	1.0261
	44	0.0001	0.0002	−0.0002	0.0000	0.0006	0.0000	0.0038	−0.1054	0.0249	0.8115
$\mathrm{NO_2\_Al_8O_{12}\_13}$	31	0.0064	0.0104	−0.0105	−0.0002	0.0407	0.0036	0.0569	0.2473	0.1278	0.9823
	32	0.0158	0.0479	−0.0352	0.0127	0.2427	0.0036	0.0565	0.1055	0.1142	1.3612
	50	0.0082	0.0088	−0.0082	0.0006	0.0379	0.0131	0.1001	0.0747	0.1511	1.0787
$\mathrm{O_2\_Al_8O_{12}\_2}$	41	0.0336	0.0432	−0.0537	−0.0104	0.1312	0.0513	0.1888	0.0110	0.2436	0.8057
$\mathrm{SO_2\_Al_8O_{12}\_2}$	37	0.0870	0.1416	−0.1583	−0.0168	0.4991	0.1072	0.2573	0.1050	0.2144	0.8940
	46	0.0006	0.0003	−0.0004	−0.0001	0.0005	0.0019	0.0436	−2.7991	0.4937	0.6490

point to a weak, non-covalent interaction between CO and $\mathrm{Al_8O_{12}}$ in the $\mathrm{CO\_Al_8O_{12}\_17}$ system. The $\mathrm{CO_2\_Al_8O_{12}\_9}$ system presents two distinct interaction scenarios at CP 36 and CP 45. At CP 36, the positive $\nabla^2\rho(\mathbf{r})$ value of 0.2646 and the very low ELF value of 0.0045 strongly suggest a closed-shell interaction, likely dominated by electrostatic forces. The positive $H(\mathbf{r})$ value of 0.0141 further supports this notion, indicating a weakly repulsive interaction. This repulsive nature could arise from steric hindrance or unfavorable electrostatic interactions between the electron clouds of $\mathrm{CO_2}$ and $\mathrm{Al_8O_{12}}$. In contrast, CP 45 exhibits a positive $\nabla^2\rho(\mathbf{r})$ value of 0.0708 and a relatively higher ELF value of 0.0292, suggesting a partially covalent character in the interaction. The negative $H(\mathbf{r})$ value of −0.0021 indicates a stabilizing interaction, implying a stronger interaction compared to CP 36. The partially covalent nature of the interaction at CP 45 suggests a greater degree of electron sharing between $\mathrm{CO_2}$ and $\mathrm{Al_8O_{12}}$, leading to a more stable interaction. The presence of two distinct interaction types within the same system highlights the complexity of the $\mathrm{CO_2\_Al_8O_{12}\_9}$ system and the potential for multiple interaction modes between $\mathrm{CO_2}$ and $\mathrm{Al_8O_{12}}$.

Both CP 30 and CP 35 in the $\mathrm{H_2\_Al_8O_{12}\_1}$ system display similar QTAIM characteristics, indicative of closed-shell interactions. The positive $\nabla^2\rho(\mathbf{r})$ values of 0.0383 and 0.0382, coupled with the low ELF values of 0.0052, suggest a lack of significant electron sharing between $\mathrm{H_2}$ and $\mathrm{Al_8O_{12}}$. The positive $H(\mathbf{r})$ value of 0.0011 further reinforces the notion of a weakly repulsive interaction. This repulsive nature is consistent with the expected behavior of a weak van der Waals interaction, where the attractive forces are counterbalanced by repulsive forces at short distances. The similarities in QTAIM parameters at both CPs suggest a consistent interaction mode between $\mathrm{H_2}$ and $\mathrm{Al_8O_{12}}$, characterized by weak, non-covalent interactions. The $\mathrm{N_2\_Al_8O_{12}\_3}$ system exhibits a predominantly closed-shell interaction at CP 41, as evidenced by the positive $\nabla^2\rho(\mathbf{r})$ value of 0.1166 and the relatively low ELF value of 0.0419. These values indicate a depletion of electron density at the BCP, characteristic of non-covalent interactions. However, the negative $H(\mathbf{r})$ value of −0.0061 suggests a weakly attractive interaction. This attractive nature could arise from weak van der Waals forces or dipole-induced dipole interactions between $\mathrm{N_2}$ and $\mathrm{Al_8O_{12}}$. The combination of a predominantly closed-shell character with a weakly attractive interaction suggests a weak, non-covalent interaction between $\mathrm{N_2}$ and $\mathrm{Al_8O_{12}}$ in the $\mathrm{N_2\_Al_8O_{12}\_3}$ system.

The $\mathrm{NO\_Al_8O_{12}\_9}$ system reveals two distinct interaction scenarios at CP 39 and CP 44. At CP 39, the positive $\nabla^2\rho(\mathbf{r})$ value of 0.0310 and the low ELF value of 0.0022 point to a closed-shell interaction, suggesting a lack of significant electron sharing between NO and $\mathrm{Al_8O_{12}}$. The positive $H(\mathbf{r})$ value of 0.0002 indicates a very weak repulsive interaction, consistent with a weak non-covalent interaction. At CP 44, the near-zero $\nabla^2\rho(\mathbf{r})$ value of 0.0006 and the ELF value of 0.0000 make it challenging to definitively characterize the interaction. However, the near-zero $H(\mathbf{r})$ value of 0.0000 suggests a very weak interaction overall. The distinct QTAIM parameters at the two CPs highlight the potential for multiple interaction modes between NO and $\mathrm{Al_8O_{12}}$, with varying strengths and characteristics. The $\mathrm{NO_2\_Al_8O_{12}\_13}$ system presents three distinct interaction scenarios at CP 31, CP 32, and CP 50. At CP 31, the positive $\nabla^2\rho(\mathbf{r})$ value of 0.0407 and the low ELF value of 0.0036 indicate a closed-shell interaction, suggesting a lack of significant electron sharing between $\mathrm{NO_2}$ and $\mathrm{Al_8O_{12}}$. The negative $H(\mathbf{r})$ value of −0.0002 suggests a weak attractive interaction. At CP 32, the positive $\nabla^2\rho(\mathbf{r})$ value of 0.2427 and the low ELF value of 0.0036 also indicate a closed-shell interaction, but the positive $H(\mathbf{r})$ value of 0.0127 suggests a weakly repulsive nature. This repulsive nature could stem from steric hindrance or unfavorable electrostatic interactions. At CP 50, the positive $\nabla^2\rho(\mathbf{r})$ value of 0.0379 and the higher ELF value of 0.0131 suggest a partially covalent interaction, indicating a greater degree of electron sharing between $\mathrm{NO_2}$ and $\mathrm{Al_8O_{12}}$. The negative $H(\mathbf{r})$ value of 0.0006 further supports a weak attractive interaction. The diverse QTAIM parameters observed at the three CPs underscore the complexity of the $\mathrm{NO_2\_Al_8O_{12}\_13}$ system and the potential for multiple interaction modes between $\mathrm{NO_2}$ and

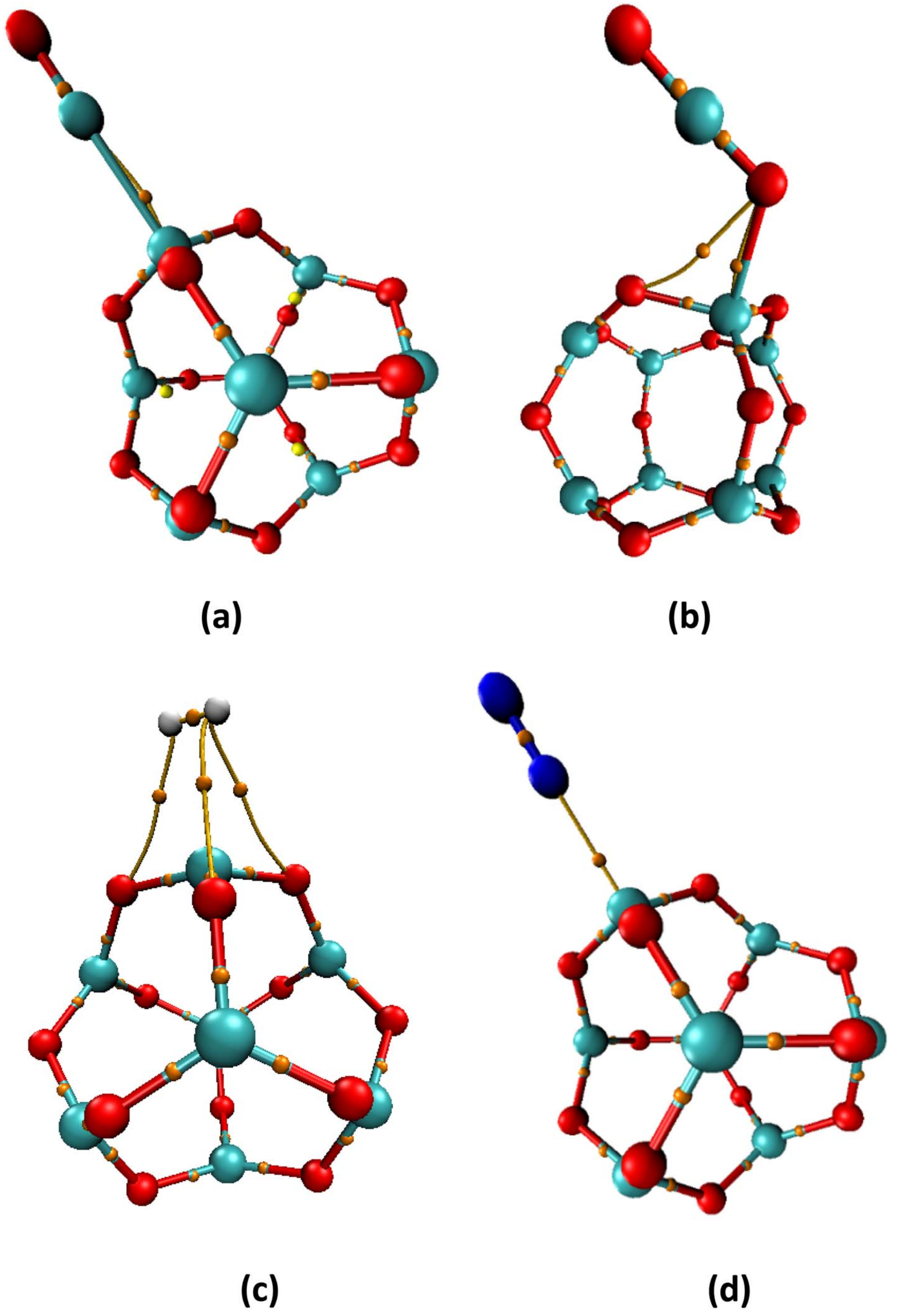

Fig. 7 Positions of the bond critical point (BCP) (3, −1) between (a) CO and (b) CO_2, (c) H_2, and (d) N_2 as well as the Al_8O_{12} cluster, are depicted that is obtained at ωB97XD/Def2TZVP level of theory.

Al_8O_{12} with varying strengths and characteristics. The O_2_Al_8O_{12}_2 system exhibits a predominantly closed-shell interaction at CP 41, as indicated by the positive $\nabla^2\rho(\mathbf{r})$ value of 0.1312 and the relatively low ELF value of 0.0513. These values suggest a lack of significant electron sharing between O_2 and Al_8O_{12}, typical of non-covalent interactions. However, the negative $H(\mathbf{r})$ value of −0.0104 suggests a weakly attractive interaction. This attractive nature could arise from weak van der Waals forces or dipole-induced dipole interactions between O_2 and Al_8O_{12}. The combination of a predominantly closed-shell character with a weakly attractive interaction point to a weak, non-covalent interaction between O_2 and Al_8O_{12} in the O_2_Al_8O_{12}_2 system. The SO_2_Al_8O_{12}_2 system displays two distinct interaction scenarios at CP 37 and CP 46. At CP 37, the positive $\nabla^2\rho(\mathbf{r})$ value of 0.4991 and the moderate ELF value of 0.1072 suggest a partially covalent interaction, indicating a greater degree of electron sharing between SO_2 and Al_8O_{12}. The negative $H(\mathbf{r})$ value of −0.0168 indicates a stabilizing interaction. At CP 46, the near-zero $\nabla^2\rho(\mathbf{r})$ value of 0.0005 and the low ELF value of 0.0019 suggest a very weak interaction. The

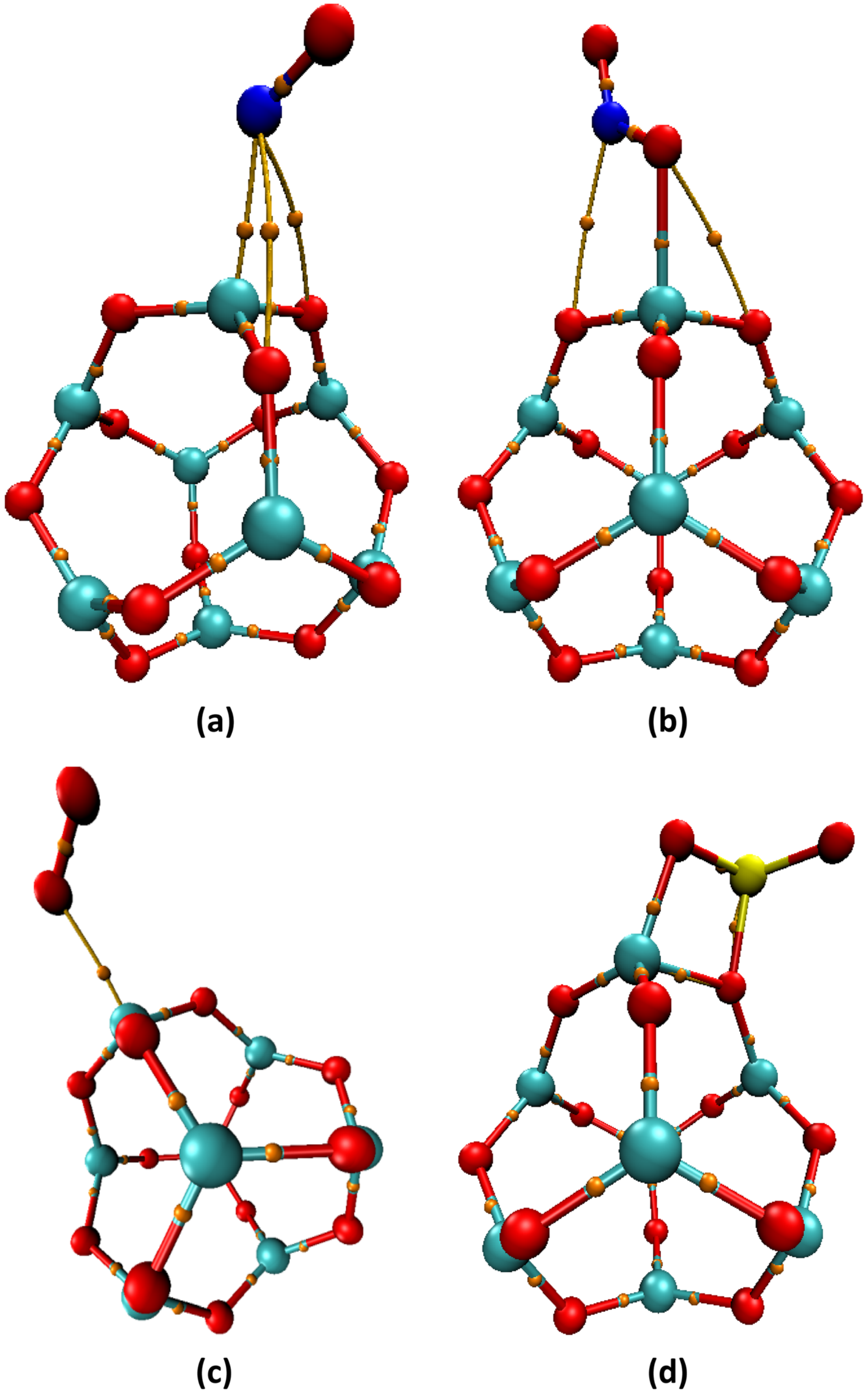

Fig. 8 Positions of the bond critical point (BCP) (3, −1) between (a) NO and (b) NO_2, (c) O_2, and (d) SO_2 as well as the Al_8O_{12} cluster, are depicted that is obtained at ωB97XD/Def2TZVP level of theory.

negative $H(\mathbf{r})$ value of −0.0001 indicates a very weak attractive interaction. The contrasting QTAIM parameters at the two CPs reveal the potential for multiple interaction modes between SO_2 and Al_8O_{12}, with varying strengths and characteristics.

The CO_Al_8O_{12}_17 system at CP 40 shows an epsilon value of 0.2995, suggesting some π-character in the interaction, and an eta value of 0.3124, indicating an asymmetrical electron density distribution and a polar bond. For CO_2_Al_8O_{12}_9, at CP 36, the high epsilon value of 0.4623 suggests a significant π-character, while the low eta value of 0.0945 points to a highly polar bond. At CP 45, the lower epsilon (0.1758) indicates less π-character and the eta value of 0.9044 suggests a more nonpolar bond. In the H_2_Al_8O_{12}_1 system, both CP 30 and 35 exhibit high epsilon values (0.4843 and 0.4914, respectively), indicating a strong π-character, and low eta values (0.1554 for both), suggesting polar bonds. The N_2_Al_8O_{12}_3 system at CP 41 displays a very low epsilon (0.0119), implying minimal π-character, and a low eta value (0.2282), suggesting a polar bond. Similarly, the NO_Al_8O_{12}_9 system shows low epsilon values at both CP 39 (0.1084) and CP 44 (0.0249), indicating weak π-character, and low eta values (0.1030 and 0.8115 respectively), implying polar bonds. The NO_2_Al_8O_{12}_13 system exhibits varying epsilon values: 0.2473 at CP 31, 0.1055 at CP 32, and 0.1511 at CP 50, suggesting varying degrees of π-character. The eta values are also diverse: 0.1278 at CP 31, 0.1142 at CP 32, and 1.0787 at CP 50, implying a range of bond polarities from polar to nearly nonpolar. The O_2_Al_8O_{12}_2 system at CP 41 has a low epsilon value (0.0110), suggesting weak π-character, and a low eta value (0.2436), indicating a polar bond. Lastly, the SO_2_Al_8O_{12}_2 system at CP 37 displays a low epsilon value (0.1050) and a low eta value (0.2144), suggesting weak π-character and a polar bond. However, at CP 46, a high epsilon (0.4937) suggests a strong π-character while the eta value of 0.6490 implies a polar bond.

3.5. NCI analysis

Non-covalent interactions, critical to various chemical and biological processes, can be analyzed using the reduced density gradient (RDG) method, which provides detailed insights into their strength and nature. RDG, calculated from the electron density (ρ) and its Laplacian ($\nabla^2\rho$), is combined with the sign function of $\lambda_2(\mathbf{r})\rho(\mathbf{r})$ to identify regions of attraction, repulsion, and weak interactions. By examining these regions, researchers can distinguish between hydrogen bonds, van der Waals forces, and other non-covalent interactions, which are essential for understanding complex molecular behaviors.

Examining the 2D RDG plots (Fig. 9 and 10) provides significant insights into the nature of molecular interactions across the studied systems. In the CO_Al_8O_{12}_17 system, the RDG plot reveals a positive Laplacian ($\nabla^2\rho$) value of 0.1230, which, in conjunction with low RDG values, indicates the presence of predominantly weak van der Waals forces. This configuration suggests a stable arrangement characterized by weak attractive interactions, reinforcing the idea that this system maintains its structure through non-covalent forces rather than strong bonding. For the CO_2_Al_8O_{12}_9 system, the RDG plot exhibits positive $\nabla^2\rho$ values, signaling weak closed-shell interactions. The increase in RDG values suggests a subtle strengthening of these interactions, indicating that while the forces remain weak, they are nonetheless becoming more significant. This gradual transition in electron density distribution implies an evolving interaction landscape that could influence the molecular stability and reactivity in the presence of varying environmental conditions. The H_2_Al_8O_{12}_1 system presents RDG plots characterized by low RDG values and positive $\nabla^2\rho$, confirming the presence of weakly attractive van der Waals interactions. This pattern suggests that although the interactions are not strong, they are sufficient to maintain molecular integrity. Such weak interactions may play a crucial role in the stability of hydrogen-bearing environments, emphasizing the significance of non-covalent forces in the system's overall behavior. In the N_2_Al_8O_{12}_3 system, positive $\nabla^2\rho$ values alongside low RDG indicate weak non-covalent interactions. This configuration reinforces the notion of stability through weak forces, although it raises questions about the potential for more robust interactions to emerge under certain conditions. The findings suggest that while the current state is stable, there may be latent interactions that could become significant under varying external influences. The NO_Al_8O_{12}_9 system shows low RDG values and a positive Laplacian, suggesting weak closed-shell interactions. However, the near-zero RDG at later points indicates diminishing electron density overlap, suggesting a shift towards a more neutral state. This evolution may have implications for the reactivity of the system, as the transition from weak attraction to neutrality could affect how the system interacts with external species or influences. In the NO_2_Al_8O_{12}_13 system, the RDG plot displays a complex interaction landscape. Positive $\nabla^2\rho$ values indicate weak attraction, but the transition to repulsive interactions as electron density evolves highlights the dynamic nature of this system. Such variability suggests that the interactions are sensitive to changes in the electronic environment, which could impact the molecular stability and reaction pathways, particularly in the context of pollutant interactions. The O_2_Al_8O_{12}_2 system presents a nuanced scenario with weak attractive interactions, marked by a positive Laplacian and low RDG values. The slight clustering in the RDG plot suggests localized regions of attraction, hinting at the potential for molecular aggregation or stabilization in specific configurations. This finding could be significant for understanding the behavior of this system under various environmental conditions. Lastly, the SO_2_Al_8O_{12}_2 system stands out with a high positive $\nabla^2\rho$ value, indicating stronger covalent interactions characterized by substantial electron density overlap. The subsequent observation of near-zero RDG and low Laplacian values suggests a transition towards very weak interactions, highlighting the complexity and variability of interactions in this system. This duality underscores the potential for both robust and weak interactions,

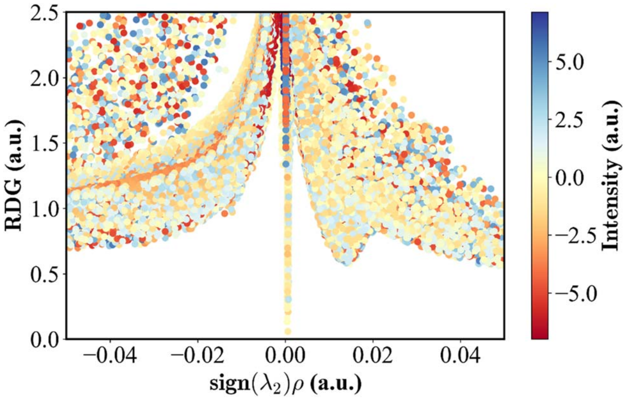

Fig. 9 The RDG *vs.* sign(λ_2)ρ(r) plot for Al_8O_{12}. The calculations are performed at ωB97XD/Def2-TZVP level of theory.

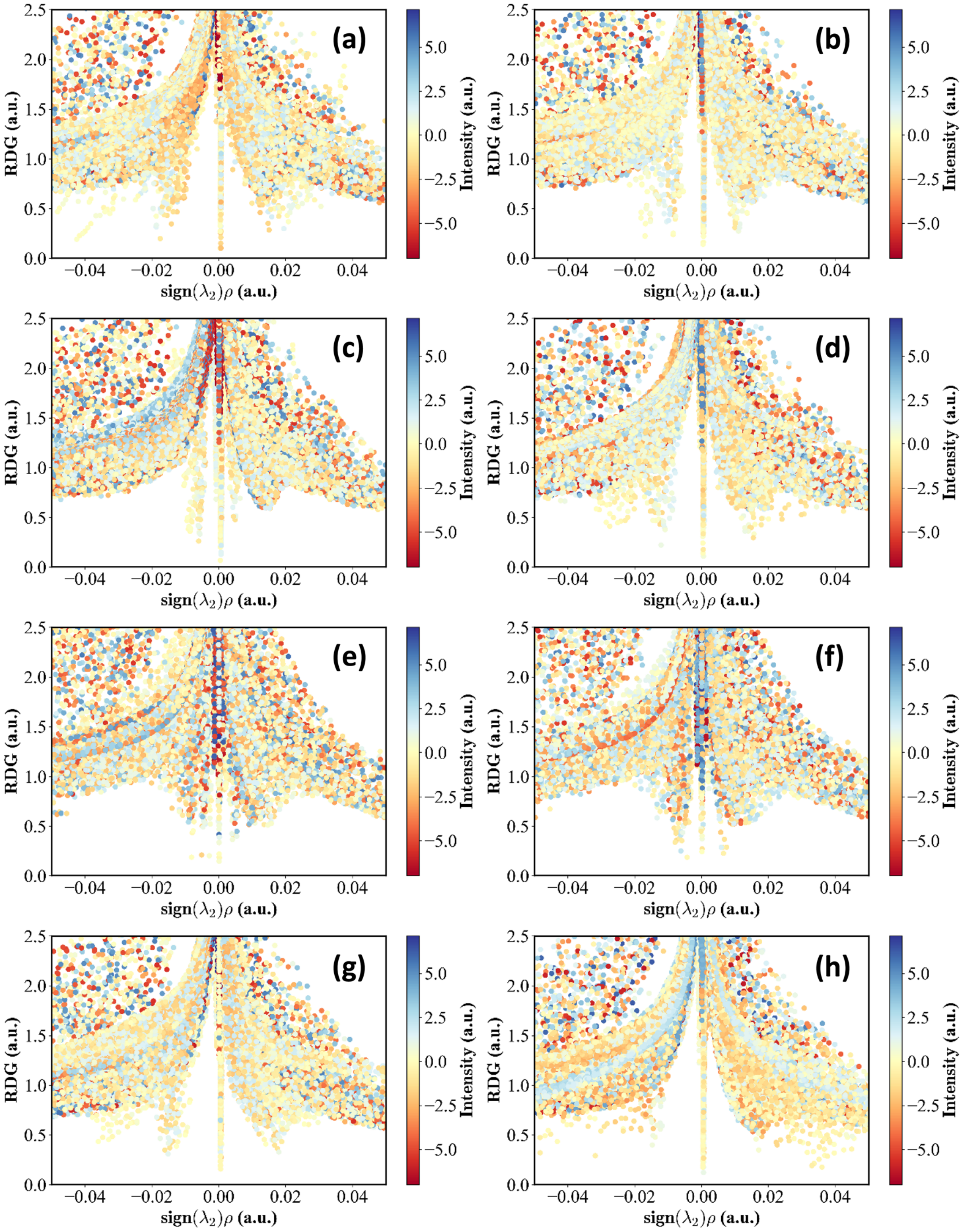

Fig. 10 The RDG *vs.* sign(λ_2)ρ(**r**) plots for (a) CO@Al_8O_{12}, (b) CO_2@Al_8O_{12}, (c) H_2@Al_8O_{12}, (d) N_2@Al_8O_{12}, (e) NO@Al_8O_{12}, (f) NO_2@Al_8O_{12}, (g) O_2@Al_8O_{12}, (h) SO_2@Al_8O_{12}. The calculations are performed at ωB97XD/Def2-TZVP level of theory.

which may be pivotal in applications involving pollutants and their interactions with environmental matrices.

4. Conclusion

The interactions between the gas molecules and the Al_8O_{12} cluster were assessed through adsorption energy calculations and various analyses, including QTAIM, TDOS, NBO, and NCI. Adsorption energies followed the trend: SO_2 > CO > CO_2 > NO_2 > O_2 > NO > N_2 > H_2, revealing strong interactions for heavier molecules. The analysis shows a clear correlation between molecular complexity and thermal properties, with larger molecules exhibiting stronger binding due to increased vibrational modes, coupling with substrate phonons, and enhanced electronic interactions. Notably, electronic effects, such as orbital overlap and molecular polarizability, dominate over size-related factors in binding strength. The Al_8O_{12} cluster maintains stability across various gas molecules, as indicated by consistent vibrational frequency shifts and predictable trends in binding energies. The strong correlation between electron-accepting capability and binding strength suggests potential for tuning adsorption properties *via* electronic structure modifications. These findings have important implications for selective gas separation, targeted storage, catalytic processes, and sensor applications. The diverse interaction profiles, ranging from weak van der Waals forces to stronger covalent bonds, demonstrate the cluster's potential for advanced gas sensing and removal, particularly in environmental monitoring. Future work could explore further optimization of the Al_8O_{12} cluster for specific applications in gas separation and sensing.

Data availability

Data will be made available on request.

Conflicts of interest

There are no conflicts to declare.

Acknowledgements

This work was supported by the National Natural Science Foundation of China (52376182, 52276189), Natural Science Foundation of Jiangsu Province (BK20221248), Project of National Center for International Research on Intelligent Nano-Materials and Detection Technology in Environmental Protection, Soochow University (SDGH2201), and Fundamental Research Funds for the Central Universities (2023JC009).

References

1 S. McArdle, S. Endo, A. Aspuru-Guzik, S. C. Benjamin and X. Yuan, *Rev. Mod. Phys.*, 2020, **92**, 015003.
2 A. Piras, C. Ehlert and G. Gryn'ova, *Comput. Mol. Biosci.*, 2021, **11**(5), e1526.
3 S. Kumar, R. Srivastava and J. Koh, *J. CO_2 Util.*, 2020, **41**, 101251.
4 D. Bonenfant, M. Kharoune, P. Niquette, M. Mimeault and R. Hausler, *Sci. Technol. Adv. Mater.*, 2008, **9**, 013007.
5 R. Morales-Salvador, J. D. Gouveia, A. Morales-Garcia, F. Vines, J. R. Gomes and F. Illas, *ACS Catal.*, 2021, **11**, 11248–11255.
6 M. Bursch, J. M. Mewes, A. Hansen and S. Grimme, *Angew. Chem., Int. Ed.*, 2022, **61**, e202205735.
7 F. Jensen, *Introduction to Computational Chemistry*, John Wiley & sons, 2017.
8 S. Fantacci, A. Amat and A. Sgamellotti, *Acc. Chem. Res.*, 2010, **43**, 802–813.
9 T. Ghanbari, F. Abnisa and W. M. A. W. Daud, *Sci. Total Environ.*, 2020, **707**, 135090.
10 J. An and N. L. Rosi, *J. Am. Chem. Soc.*, 2010, **132**, 5578–5579.
11 K. T. Butler, J. M. Frost, J. M. Skelton, K. L. Svane and A. Walsh, *Chem. Soc. Rev.*, 2016, **45**, 6138–6146.
12 J. Hafner, C. Wolverton and G. Ceder, *MRS Bull.*, 2006, **31**, 659–668.
13 M. D. Mohammadi, H. Y. Abdullah, H. Louis, E. E. Etim, H. O. Edet and O. C. Godfrey, *Chemical Physics Impact*, 2023, **6**, 100234.
14 V. Barone, O. Hod, J. E. Peralta and G. E. Scuseria, *Acc. Chem. Res.*, 2011, **44**, 269–279.
15 M. Cossi, N. Rega, G. Scalmani and V. Barone, *J. Comput. Chem.*, 2003, **24**, 669–681.
16 Y. Zeng, R. Zou and Y. Zhao, *Adv. Mater.*, 2016, **28**, 2855–2873.
17 J. Ozdemir, I. Mosleh, M. Abolhassani, L. F. Greenlee, R. R. Beitle Jr and M. H. Beyzavi, *Front. Energy Res.*, 2019, **7**, 77.
18 S. Malola and H. Häkkinen, *Nat. Commun.*, 2021, **12**, 2197.
19 D. Ghelani and S. Faisal, 2022, DOI: 10.22541/au.166490972.20428974/v1.
20 O. Tillement, S. Illy-Cherrey, J. Dubois, S. Begin-Colin, F. Massicot, R. Schneider, Y. Fort, J. Ghanbaja, C. Bellouard and E. Belin-Ferre, *Philos. Mag. A*, 2002, **82**, 913–923.
21 S. R. Desai, H. Wu, C. M. Rohlfing and L.-S. Wang, *J. Chem. Phys.*, 1997, **106**, 1309–1317.
22 Y. K. Park, E. H. Tadd, M. Zubris and R. Tannenbaum, *Mater. Res. Bull.*, 2005, **40**, 1506–1512.
23 N. Khare, D. Hesterberg and J. D. Martin, *Environ. Sci. Technol.*, 2005, **39**, 2152–2160.
24 A. M. Scheidegger, G. M. Lamble and D. L. Sparks, *J. Colloid Interface Sci.*, 1997, **186**, 118–128.
25 B. P. Dhonge, T. Mathews, S. T. Sundari, C. Thinaharan, M. Kamruddin, S. Dash and A. Tyagi, *Appl. Surf. Sci.*, 2011, **258**, 1091–1096.
26 C. Nurcahyani, A. E. Anjani, A. Purwanto, C. S. Yudha, L. M. Hasanah, E. R. Dyartanti and A. Nur, *AIP Conf. Proc.*, 2020, **2219**, 030003.
27 M. Lindner and M. Schmid, *Coatings*, 2017, **7**, 9.
28 D. M. Mattox, *Handbook of Physical Vapor Deposition (PVD) Processing*, William Andrew, 2010.
29 Y. Berkovich, A. Aserin, E. Wachtel and N. Garti, *J. Colloid Interface Sci.*, 2002, **245**, 58–67.
30 D. Al-Mawlawi, C. Liu and M. Moskovits, *J. Mater. Res.*, 1994, **9**, 1014–1018.
31 S. Thomas and P. M. Sherwood, *Anal. Chem.*, 1992, **64**, 2488–2495.
32 G. E. J. Poinern, N. Ali and D. Fawcett, *Materials*, 2011, **4**, 487–526.
33 R. L. Whetten, H.-C. Weissker, J. J. Pelayo, S. M. Mullins, X. López-Lozano and I. L. Garzón, *Acc. Chem. Res.*, 2019, **52**, 34–43.
34 B. Wang, J. Zhao, X. Chen, D. Shi and G. Wang, *Phys. Rev. A*, 2005, **71**, 033201.
35 B. Weinert, S. Mitzinger and S. Dehnen, *Chem.–Eur. J.*, 2018, **24**, 8470–8490.
36 J. Zhang and M. Dolg, *Phys. Chem. Chem. Phys.*, 2015, **17**, 24173–24181.
37 J.-D. Chai and M. Head-Gordon, *J. Chem. Phys.*, 2008, **10**, 6615–6620.
38 A. S. Rad and K. Ayub, *Mol. Phys.*, 2017, **115**, 879–884.
39 P. Karamanis, *Int. J. Quantum Chem.*, 2012, **112**, 2115–2125.

40 T. Udagawa, K. Suzuki and M. Tachikawa, *Procedia Comput. Sci.*, 2017, **108**, 2275–2281.
41 F. Weigend and R. Ahlrichs, *Phys. Chem. Chem. Phys.*, 2005, **7**, 3297–3305.
42 J. C. Poutsma, W. Moeller, J. L. Poutsma, B. C. Sweeny, S. G. Ard, A. A. Viggiano, *et al.*, *J. Phys. Chem. A*, 2022, **126**, 1648–1659.
43 M. Khatun, P. Sarkar, S. Panda, L. T. Sherpa and A. Anoop, Nanoclusters and Nanoalloys of Group 13 elements B, Al, and Ga: Benchmark, structure, and property analysis, *Phys. Chem. Chem. Phys.*, 2023, **25**, 19986–20000.
44 S. Shi, Y. Liu, C. Zhang, B. Deng and G. Jiang, *Comput. Theor. Chem.*, 2015, **1054**, 8–15.
45 P. L. Rodríguez-Kessler, *arXiv*, 2024, preprint, arXiv:2408.16651, DOI: 10.48550/arXiv.2408.16651.
46 J. Antony, R. Sure and S. Grimme, *Chem. Commun.*, 2015, **51**, 1764–1774.
47 S. Grimme, J. Antony, T. Schwabe and C. Mück-Lichtenfeld, *Org. Biomol. Chem.*, 2007, **5**, 741–758.
48 M. J. Frisch, G. W. Trucks, H. B. Schlegel, G. E. Scuseria, M. A. Robb, J. R. Cheeseman, G. Scalmani, V. Barone, G. A. Petersson, H. Nakatsuji, X. Li, M. Caricato, A. V. Marenich, J. Bloino, B. G. Janesko, R. Gomperts, B. Mennucci, H. P. Hratchian, J. V. Ortiz, A. F. Izmaylov, J. L. Sonnenberg, D. Williams-Young, F. Ding, F. Lipparini, F. Egidi, J. Goings, B. Peng, A. Petrone, T. Henderson, D. Ranasinghe, V. G. Zakrzewski, J. Gao, N. Rega, G. Zheng, W. Liang, M. Hada, M. Ehara, K. Toyota, R. Fukuda, J. Hasegawa, M. Ishida, T. Nakajima, Y. Honda, O. Kitao, H. Nakai, T. Vreven, K. Throssell, J. A. Montgomery Jr, J. E. Peralta, F. Ogliaro, M. J. Bearpark, J. J. Heyd, E. N. Brothers, K. N. Kudin, V. N. Staroverov, T. A. Keith, R. Kobayashi, J. Normand, K. Raghavachari, A. P. Rendell, J. C. Burant, S. S. Iyengar, J. Tomasi, M. Cossi, J. M. Millam, M. Klene, C. Adamo, R. Cammi, J. W. Ochterski, R. L. Martin, K. Morokuma, O. Farkas, J. B. Foresman and D. J. Fox, *Gaussian 16, Revision C.01*, Gaussian, Inc., Wallingford CT, 2016.
49 F. Weinhold, C. Landis and E. Glendening, *Int. Rev. Phys. Chem.*, 2016, **35**, 399–440.
50 T. Lu and F. Chen, *J. Comput. Chem.*, 2012, **33**, 580–592.
51 R. Dennington, T. A. Keith and J. M. Millam, *GaussView, Version 6.1*, Semichem Inc., Shawnee Mission, KS, 2016.
52 Z. Fang, Y. Wang and D. A. Dixon, *J. Phys. Chem. C*, 2015, **119**, 23413–23421.
53 M. Born and J. Mayer, *Z. Phys.*, 1932, **75**, 1–18.
54 G. Lewis and C. Catlow, *J. Phys. C:Solid State Phys.*, 1985, **18**, 1149.
55 G. Herzberg, *Molecular Spectra and Molecular Structure*, 1950, **1**, 127.
56 D. F. Blyth, PhD Thesis, University of St. Andrews, United Kingdom, 1996.
57 J. Q. Wang, J. Sun, W. G. Cheng, K. Dong, X. P. Zhang and S. J. Zhang, *Phys. Chem. Chem. Phys.*, 2012, **14**, 11021–11026.
58 J.-L. Bredas, *Mater. Horiz.*, 2014, **1**, 17–19.
59 P. Hohenberg and W. Kohn, *Phys. Rev.*, 1964, **136**, B864.
60 P. Geerlings, S. Fias, Z. Boisdenghien and F. De Proft, *Chem. Soc. Rev.*, 2014, **43**, 4989–5008.
61 M. Doust Mohammadi and H. Y. Abdullah, *Struct. Chem.*, 2022, 1–16.
62 M. D. Mohammadi, H. Y. Abdullah, V. G. Kalamse and A. Chaudhari, *Comput. Theor. Chem.*, 2022, **1208**, 113544.
63 M. Doust Mohammadi and H. Y. Abdullah, *Bull. Mater. Sci.*, 2022, **45**, 33.
64 M. D. Mohammadi, F. Abbas, H. Louis, L. E. Afahanam and T. E. Gber, *ChemistrySelect*, 2022, **7**, e202202535.
65 P. K. Chattaraj and S. Giri, *Annu. Rep. Prog. Chem., Sect. C:Phys. Chem.*, 2009, **105**, 13–39.
66 P. Geerlings, F. De Proft and W. Langenaeker, *Chem. Rev.*, 2003, **103**, 1793–1874.
67 D. Chakraborty and P. K. Chattaraj, *Chem. Sci.*, 2021, **12**, 6264–6279.
68 Z. Yan, Y. Zhang, W. Kang, N. Deng, Y. Pan, W. Sun, J. Ni and X. Kang, *Nanomaterials*, 2022, **12**, 3611.